JGR Solid Earth

RESEARCH ARTICLE
10.1029/2021JB022201

New Insights Into the Rift to Drift Transition Across the Northeastern Nova Scotian Margin From Wide-Angle Seismic Waveform Inversion and Reflection Imaging

Hanchao Jian[1,2,3], Mladen R. Nedimović[1,2], Juan Pablo Canales[3], and K. W. Helen Lau[1]

[1]Department of Earth and Environmental Sciences, Dalhousie University, Halifax, NS, Canada, [2]Ocean Frontier Institute, Dalhousie University, Halifax, NS, Canada, [3]Department of Geology and Geophysics, Woods Hole Oceanographic Institution, Woods Hole, MA, USA

Key Points:

- We derive coincident velocity and reflection sections by waveform inversion of wide-angle and depth migration of near-offset seismic data
- Intermittent magmatism accompanying lithospheric breakup and onset of seafloor spreading is imaged in a presumed amagmatic rift segment
- Thin incipient oceanic crust formed by magma-poor spreading overlies serpentinized mantle seaward from the imaged continent-ocean boundary

Supporting Information:

Supporting Information may be found in the online version of this article.

Correspondence to:

H. Jian,
hjian@whoi.edu

Citation:

Jian, H., Nedimović, M. R., Canales, J. P., & Lau, K. W. H. (2021). New insights into the rift to drift transition across the northeastern Nova Scotian margin from wide-angle seismic waveform inversion and reflection imaging. *Journal of Geophysical Research: Solid Earth*, *126*, e2021JB022201. https://doi.org/10.1029/2021JB022201

Received 14 APR 2021
Accepted 14 NOV 2021

Abstract Sparse wide-angle seismic profiling supported by coincident reflection imaging has been instrumental for advancing our knowledge about rifted margins. Nevertheless, features of critical importance for understanding rifting processes have been poorly resolved. We derive a high-resolution velocity model by applying full waveform inversion to the dense OETR-2009 wide-angle seismic profile crossing the northeastern Nova Scotian margin. We then create a coincident reflection image by prestack depth migrating the multichannel seismic data. This allows for the first detailed interpretation of the structures related to the final stages of continental breakup and incipient oceanic accretion at the Eastern North America Margin. Our interpretation includes a hyperextended continental domain overlying partially serpentinized mantle, followed by a 10-km-wide domain consisting of a continental block surrounded by layered and bright reflectors indicative of magmatic extrusions. A major fault, representing the continent-ocean boundary, marks a sharp seaward transition to a 16-km-wide domain characterized by smoother basement with chaotic reflectors, where no continental materials are present and a 3-km-thick embryonic oceanic crust overlying partially serpentinized mantle is created by the breakup magmatism. Further seaward, thin oceanic crust overlies the serpentinized mantle suggesting magma-poor oceanic spreading with variable magma supply as determined from variable basement topography, 2–4 km thick volcanic layer, and magnetic anomalies. Our results demonstrate that magmatism played an important role in the lithospheric breakup of the area crossed by the OETR-2009 profile. Considering that the northeastern Nova Scotian margin has been classified as amagmatic, large margin-parallel variations in magma supply likely characterize a single rift segment.

Plain Language Summary The Atlantic Ocean was born from the breakup of the supercontinent Pangea at ~200 million years ago. The >30 km-thick continental crust is thinned to zero, and then oceanic crust is accreted via the interplay of tectonic extension and magmatic addition originated from mantle upwelling and melting. The continental margins around the Atlantic Ocean record the process of continent-ocean transition (COT), showing great diversity that can be ascribed to the amount and timing of magmatism during the COT process. Offshore northeastern Nova Scotia, the rifted margin is thought to be magma-poor. When and how oceanic spreading with magmatic materials emplaced in the crust began are not clear. In this study, we derive high-resolution seismic models of the crustal and upper mantle structure offshore northeastern Nova Scotia. We discover a short-period magmatic event accompanying the final continent breakup, marking the boundary between the hype-thinned continental crust and the embryonic oceanic crust. Seaward of the boundary is interpreted as oceanic spreading domain with variable, but overall small-amount magma supply. Our results demonstrate that even at magma-poor margins, magmatism accompanies the continental breakup and onset of seafloor spreading, and the mantle upwelling and melting starts prior to the final continental breakup.

1. Introduction

Magmatism greatly affects the style of continental breakup, to the point where rifted continental margins are broadly categorized as magma-rich and magma-poor types (Louden et al., 2013; Tugend et al., 2020). Seismic observations at magma-rich margins, such as the eastern US seaboard (e.g., Holbrook & Kelemen, 1993), commonly reveal a continent-ocean transition (COT) with thicker than average transitional crust due to lower-crustal igneous underplating or intrusions and subaerial lava flows (e.g., Hinz et al., 1987; Quirk et al., 2014; Voss et al., 2009) that result from early inception of decompression melting during continental rifting (Guan

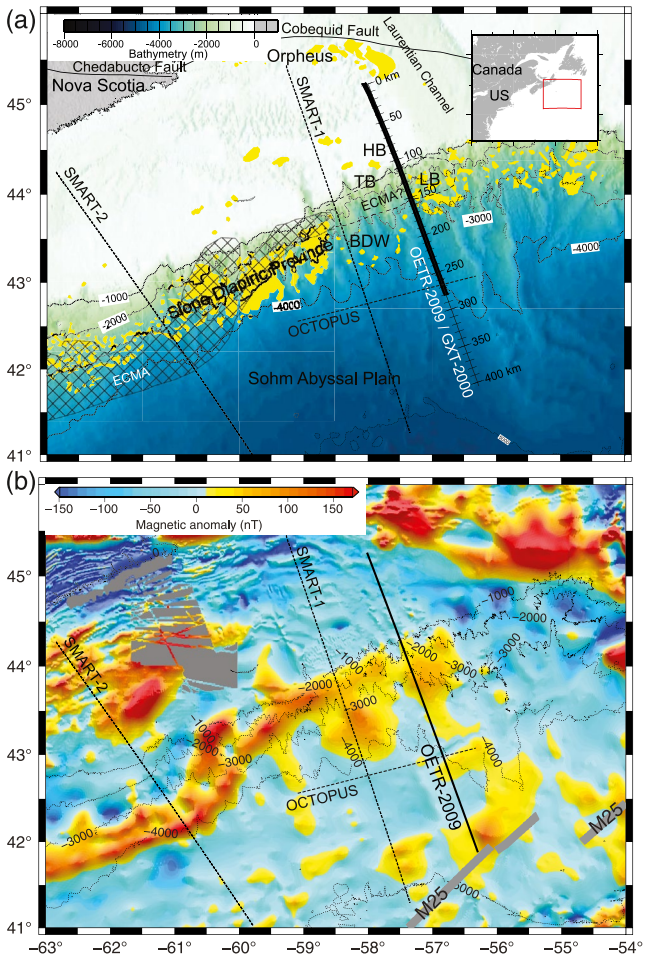

Figure 1. Study area and seismic profiles. (a) Bathymetry map of the northeastern Nova Scotian continental margin with the location of the OETR-2009 (Lau et al., 2018), OCTOPUS (Lau et al., 2019), and SMART 1 and 2 (Funck et al., 2004; Wu et al., 2006) wide-angle seismic profiles. The numbers alongside the OETR-2009 profile indicate along-profile distance from the landward end, as used in the data analysis. The thick black line shows the coincident multichannel seismic profile extending from 0 to 280 km distance. Yellow spots indicate salt bodies (Shimeld, 2004). Diamond-patterned region is the East Coast Magnetic Anomaly (ECMA) with the black dashed curve outlining its recently proposed eastward continuation (Sibuet et al., 2012). HB: Huron Basin; TB: Tantallon; LB: Laurentian Basin; and BDW: Banquereau Detachment Wedge. (b) Magnetic anomaly map. Data are from Oakey and Dehler (2004). Thin black curves are depth contours of the bathymetry. The M25 magnetic anomaly is originally picked by Klitgord and Schouten (1986) and interpolated by Seton et al. (2020).

et al., 2021; Tugend et al., 2020). Magma-poor margins show wider transition zones resulting from a less uniform breakup process that leaves asymmetric structures between the conjugate margin pairs. Some of the well-studied magma-poor margins, such as the Newfoundland–Iberia, Flemish Cap–Galicia Bank, and Flemish Cap–Goban Spur conjugates show that partially serpentinized mantle overlain by hyperextended continental crust or exhumed highly serpentinized mantle, is pervasive in the wide COT zone (e.g., Chian et al., 1999; Gerlings et al., 2012; Pickup et al., 1996; Tucholke et al., 2007; Van Avendonk et al., 2006; Welford et al., 2010). Nevertheless, recent studies argue that even at magma-poor margins small amounts of magmatism are present and lead to the final continental breakup and the onset of seafloor spreading (Bronner et al., 2011; Gillard et al., 2017; Tugend et al., 2020; Whitmarsh et al., 2001).

The Nova Scotian margin (Figure 1a) sits at a transition between the magma-rich margin of the Eastern US to the south and the magma-poor Newfoundland margin to the north (Dehler & Welford, 2013; Keen & Potter, 1995; Louden et al., 2013). The northward weakening of the East Coast Magnetic Anomaly (ECMA) indicates decreasing synrift magmatism in this direction (Figure 1b). Margin-normal wide-angle seismic profiling using ocean bottom seismometers (OBS) confirms the northward magma-rich to magma-poor margin-parallel transition at a regional scale (Dehler, 2012; Funck et al., 2004; Lau et al., 2018; Wu et al., 2006), firmly putting the northeastern Nova Scotian margin (Figure 1) in the magma-poor category. Funck et al. (2004) interpret hyperextended continental crust and highly serpentinized mantle exhumed in the COT zone along the SMART-1 profile (Figure 1). Along the OETR-2009 profile (Figure 1), Lau et al. (2018) identify a similar COT zone except with no mantle exhumation (Figure 2a). This along-margin structural complexity of the COT at the northeastern Nova Scotian margin is further supported by OCTOPUS, a margin-parallel OBS profile that runs along the COT, crosses both the SMART-1 and OETR-2009 profiles and displays highly variable short-wavelength (~50 km) crystalline basement structures (Lau et al., 2019). In both the SMART-1 and OETR-2009 models, thinner than normal oceanic crust is imaged and interpreted as juxtaposed with the COT crust, but the more detailed information about the onset of seafloor spreading and the role of magmatism in the breakup has not yet been captured due to data and/or imaging limitations. In order to better understand the rift to drift transition, we use an advanced data analysis approach to revisit the OETR-2009 data set, which is by far of the highest data density among crustal-scale wide-angle seismic experiments offshore Nova Scotia and among the top globally.

The OETR-2009 profile has been previously analyzed using the RAYINVR layered modeling approach (Zelt & Smith, 1992), which assumes vertically linear velocity variations within the layers. By incorporating the interfaces picked from a coincident high-quality seismic reflection image (Lau et al., 2018), the layered modeling method can handle the sedimentary structures pretty well. However, the modeling of subbasement layers can be subjective because of the lack of intrabasement reflectors and strong variations in the vertical velocity gradient. The model resolution is also limited because the model can only be coarsely parameterized as interface locations and velocities at layer boundaries.

In this study, we adopt a multi-scale inversion method that aims to retrieve a minimum-structure model by progressively increasing model complexity until the data are fit to a desired level. The dependence on a priori information is minor because we make no assumptions regarding the Moho or other intrabasement boundaries, and the resolution is high as the models are discretized using fine grids (Van Avendonk et al., 2006; Zelt et al., 2003).

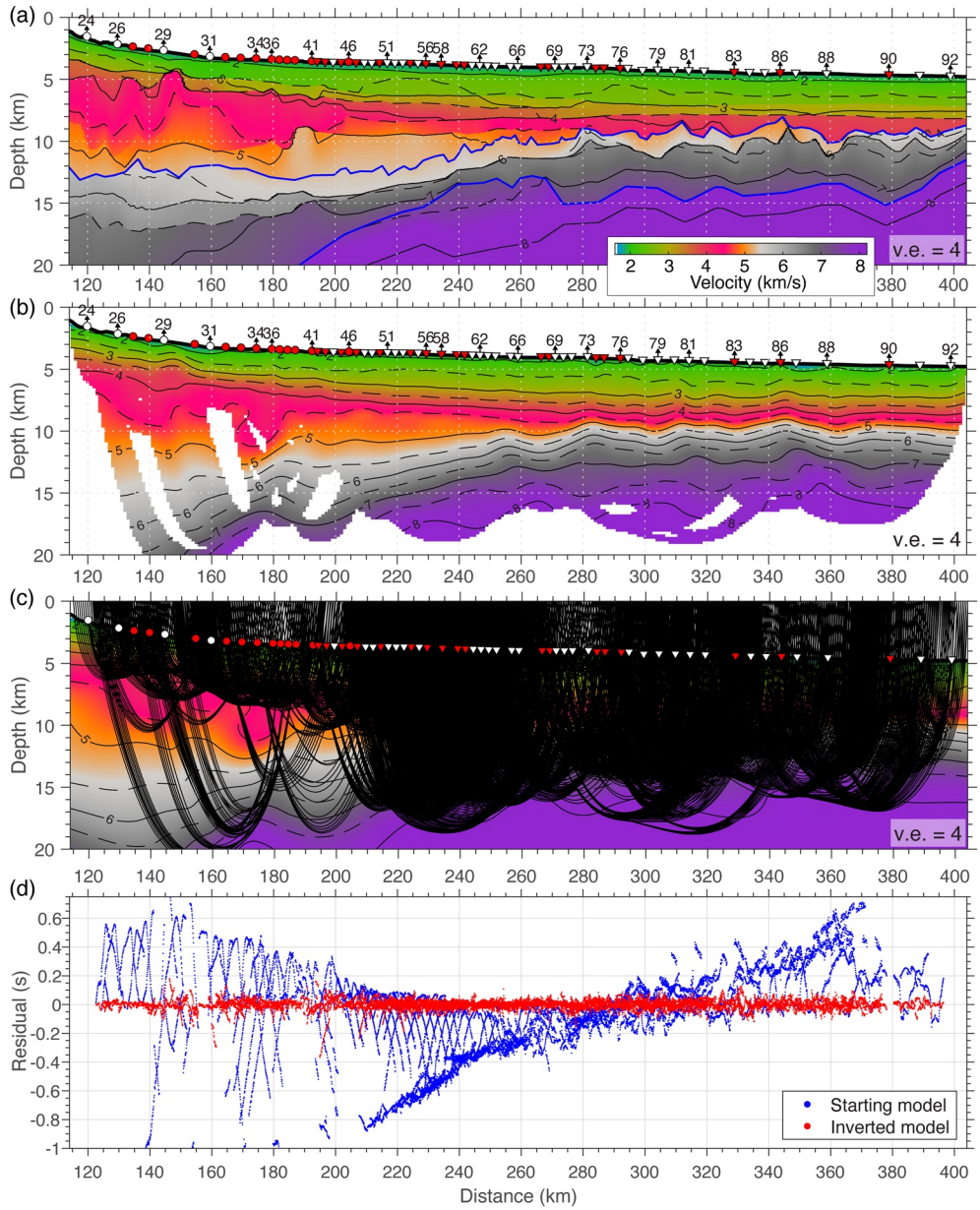

Figure 2. Traveltime tomography of the ocean bottom seismometer (OBS) data. (a) Layered model from Lau et al. (2018). The blue lines indicate the top basement and Moho interface in the layered model. (b) Inverted first-arrival traveltime tomography (FAT) model with the unconstrained nodes masked in white. (c) Ray paths (black) calculated from the FAT model, which are decimated by a factor of 5 for clarity. The vertical exaggeration in (a–c) is 4. We use data recorded by deep-water OBS instruments that are marked as circles and triangles, which were deployed during two shooting phases, respectively. Red color indicates OBSs with good-quality records on both hydrophone and vertical channels, whereas white color indicates OBSs whose vertical geophone failed to record seismic signals. OBS numbers sequentially increase seaward. (d) Data residuals for the starting model and the inverted model in the FAT. The RMS residual is reduced from about 280 ms to about 32 ms after the inversion, which is close to the picking uncertainty.

Our multi-scale approach includes a combination of first-arrival traveltime tomography (FAT) (Van Avendonk et al., 2004) and full waveform inversion (FWI) (Shipp & Singh, 2002) methods. The FAT resolves long-wavelength structures that serve as a starting model for the FWI, which then improves the model resolution through fitting the full waveform information. Based on the FWI velocity model, we also performed prestack depth migration using coincident long-streamer multi-channel seismic (MCS) data. Our study is one of the first to employ such a multi-scale seismic imaging method to investigate the structure of a rifted margin. The only comparably

detailed imaging study so far carried out at a rifted margin, though on shorter profile (~60 vs. ~170 km in this work), was carried out at the Deep Galicia Margin (Davy et al., 2016, 2018).

In the following sections, we first briefly review the geological background and describe the OETR-2009 wide-angle OBS data. We then present the FAT and FWI methods used, the computed results, and the reflection imaging. Finally, we interpret all the results and discuss their implication on the rift to drift transition and early oceanic spreading processes.

2. Geological Background

The conjugate Nova Scotian and Moroccan continental margin pair was created by the Mesozoic rifting of Pangea that started in the Late Triassic (about 230 Ma) and continued until the Early Jurassic (about 175 Ma) (Klitgord & Schouten, 1986). The detailed age of continental breakup and onset of oceanic spreading at the Nova Scotian margin is of great uncertainties, because the M25 isochron (~155 Ma; Ogg et al., 2016) lies >250 km away from the ECMA (~190 Ma; Sibuet et al., 2012) and no other magnetic anomalies are identified between them. The continental lithosphere of both margins formed during the Paleozoic Appalachian Orogen. Onshore on the Scotian side, the west-east Cobequid Chedabucto fault separates the Avalon terrane to the north (Barr & Raeside, 1989) and the Meguma terrane (Williams, 1995) to the south, the latter of which comprises much of the margin (Figure 1a). Offshore, the deep basins are filled by up to about 15 km of sediment. Salt diapirs are widely observed in the Slope Diapiric Province (Deptuck & Kendell, 2017; Shimeld, 2004) (Figure 1a).

The high-amplitude ECMA (200–300 nT; Figure 1b) on the southwestern part of the margin is explained by synrift volcanic extrusive bodies, as supported by the seaward dipping reflectors on seismic images (Keen & Potter, 1995) that are indicative of magma-rich rifting. The ECMA seems to split up into weaker (180 nT) and thinner lineations offshore central Nova Scotia (Dehler, 2012). Further northeast, it continues to dissipate and disperses into large spots with much weaker amplitudes (50–80 nT). Similar speckled and weak magnetic anomalies are distributed further seaward, including the M25 anomaly (Figure 1b). Those weak magnetic anomalies may be attributed to a smaller amount of magmatic accretions or serpentinization process under magma-poor rifting or slow/ultraslow spreading circumstances (e.g., Bronner et al., 2014; Sauter et al., 2008; Sibuet et al., 2007). No matter what causes these anomalies, the scattered distribution of these anomalies suggests a three-dimensional (3-D) variation of the rifting/spreading processes, similar to what is observed at the slow/ultraslow spreading mid-ocean ridges (Lin et al., 1990).

3. Data and Methods

3.1. Wide-Angle Seismic Data and Processing

During the OETR-2009 wide-angle seismic experiment there were 100 OBS deployments, out of which 78 OBSs recorded useful data (Lau et al., 2018). The OBS spacing ranges from <3 km to >10 km, with the highest instrument density over the COT (Figure 2a). All instruments were equipped with a three-component geophone and a hydrophone. Of particular interest for our work are the data recorded by the vertical geophones and hydrophones, as our intention is to develop P-wave velocity models. The vertical geophone data are generally less affected by noise produced by ocean waves and thus, commonly show better signal-to-noise ratios than the corresponding hydrophone data (e.g., Figure 3). However, in this experiment, vertical geophones in about half of the OBSs failed to record any data. These OBS are marked in Figures 2a–2c with white color, as opposed to the OBSs marked with red that recorded data on both the vertical geophone and hydrophone channels. To get as much information as possible from the data, we incorporate both channels in our analysis.

We start from the data that have been converted to SEG-Y format and corrected for linear clock drifts (Lau et al., 2018). We first conduct OBS relocations by performing grid searches for the OBS locations and static time shift searches that combined, provide the best fits for picked direct wave traveltimes. The final root-mean-square (RMS) residual is less than 4 ms, that is, the OBS sampling interval, for 80% instruments, and less than 8 ms for all instruments. The posteriori probability distribution indicates that the along-profile location is very well constrained, where a shift of 10 m would increase the RMS misfit by >4 ms. In contrast, the cross-profile location and depth are weakly constrained due to the lack of 3-D direct-wave ray coverage. Although the maximum cross-profile distances obtained by the relocations are about 1 km, most of them (over 90%) are less than 500 m.

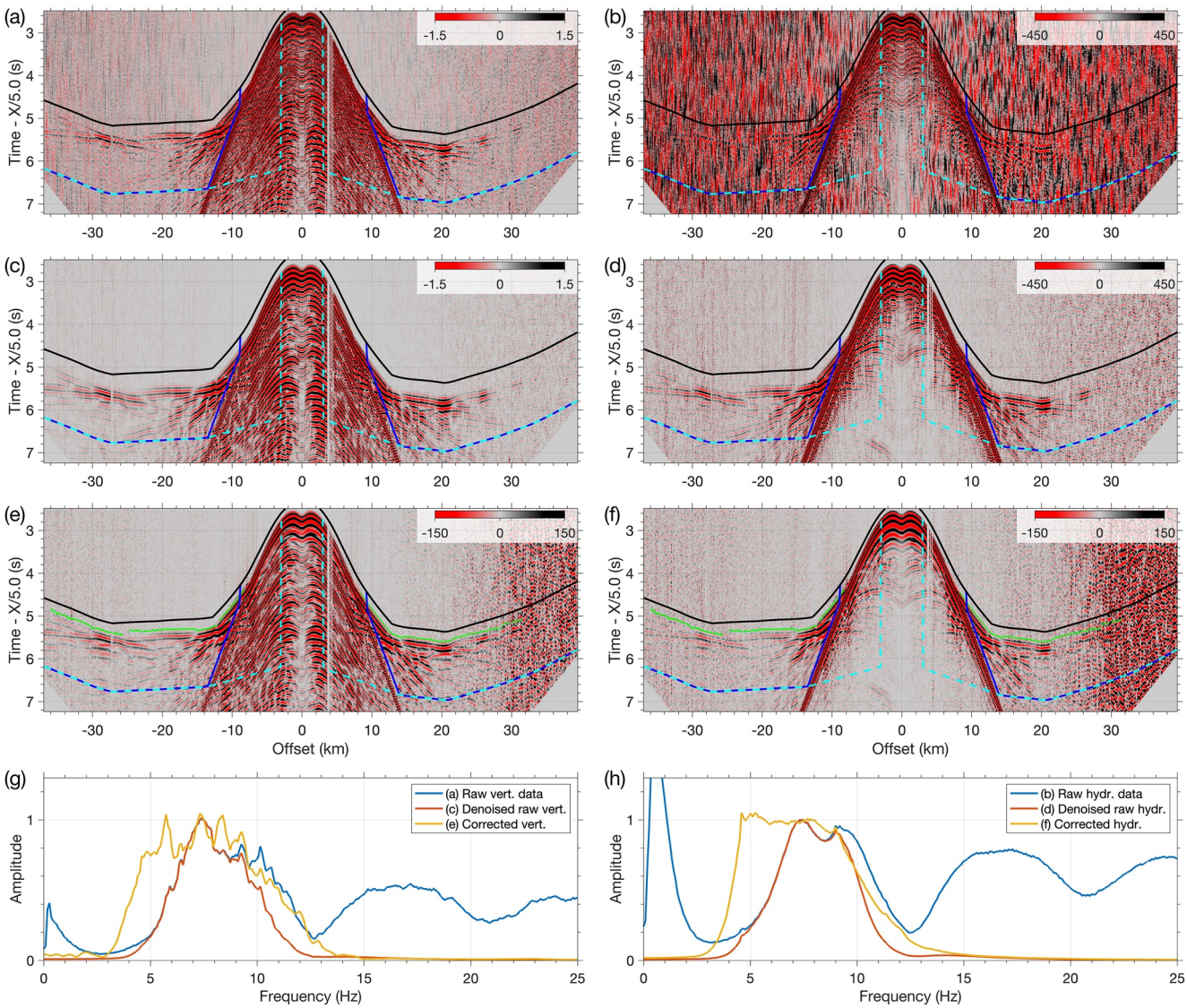

Figure 3. The ocean bottom seismometer (OBS) data preprocessing example: the vertical (a, c, e, and g) and hydrophone (b, d, f, and h) channel records of OBS 59. (a and b) Raw data. (c and d) Data after a Butterworth filter with corner frequencies at 4.5 and 10 Hz. (e and f) Processed data after application of the shaping filters and a Butterworth filter between 4.5 and 10 Hz. All data traces are scaled with the square root of offset for display purposes. Green curves in (e and f) mark the hand-picked first arrivals. Black curves in (a–f) indicate the upper boundary of the mute window for full waveform inversion (FWI), designed based on the predicted first-arrival traveltimes. Dashed cyan and solid blue curves depict the lower boundary of the FWI mute window, which are chosen to select mid- and long-offset and only long-offset wide-angle arrivals, respectively. (g and h) Amplitude spectra of (a–f) that are normalized at 7.5 Hz. Note the wider and flatter signal spectra in the frequency domain after the processing and the corresponding wave trains in the time domain that show much reduced ringing.

An array of eight airguns (total volume of 64 L) was fired every 60 s to generate seismic energy. However, the emitted signals were not consistent throughout the OBS experiment due to bad weather and unstable performance of the airguns and compressors. It is important to ameliorate these source inconsistencies before the inversion of the OBS data. Because no far-field records of source signatures are available, we exploit the near-offset (<3 km) direct waves in OBS hydrophone data as analogs to far-field source signatures. The amplitudes of the direct wave recordings are compensated for geometrical spreading effect using their travel times, assuming that water is a homogeneous and non-dissipative medium and the interference of seafloor reflections is negligible at the low frequencies of interest. The later assumption is relaxed as the offset dependence of the interference is negligible for the near offsets, because we incorporate a source signature correction in the FWI. These assumptions are validated by the consistency between source signatures extracted from different neighboring OBSs (Figure 4a).

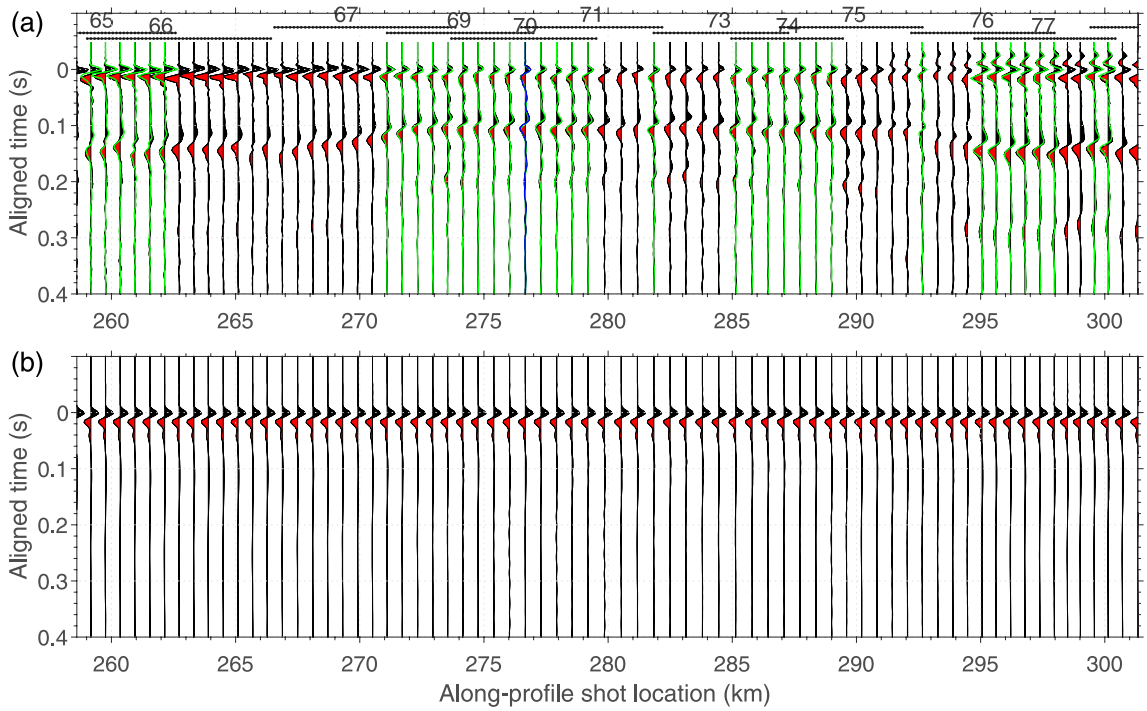

Figure 4. Shot signature correction. (a) Example of raw shot signatures extracted from the near-offset direct water wave arrivals after compensation for geometrical spreading, showing significant inconsistencies. Horizontal lines and numbers on the top indicate the ocean bottom seismometer (OBS) from which the signature is extracted. Wiggles and positive variable areas are black and negative variable areas are red. When data from more than one OBS are available for a shot, the data traces (wiggles) from the 2nd and 3rd OBS are plotted in green and blue colors, respectively. The shots are decimated by a factor of 4 for clarity. (b) The corresponding output signatures after application of the shaping filters.

Figure 4a shows examples of the extracted source signatures, indicating significant variations in both amplitude and shape. Additionally, bubble sequences are observed as recurrent energy packages following the first break in the source signatures (Figure 4a), and in the low-frequency wide-angle phases they appear as long wave trains that obscure later arrivals (Figures 3a–3d). These bubbles cause notches in amplitude spectra that strongly affect low frequencies, narrowing the frequency band that can be used in the waveform inversion (Figures 3g and 3h). For example, bubble sequences repeating every 125 ms would introduce amplitude valleys every 8 Hz at 4, 12, and 20 Hz, etc. In order to eliminate source inconsistencies and bubble sequences, we adopt a deterministic deconvolution method of Wood et al. (1978) to shape the raw source signatures to a band-limited spike between 3 and 40 Hz. The resulting source signatures are shown in Figure 4b. These shaping filters are then applied on corresponding data traces. Figures 3e and 3f illuminate the effect on wide-angle phases using the OBS 59 record as an example. In both the hydrophone and vertical geophone data, the shaping filters effectively eliminate source inconsistencies and enhance low frequencies in the data that are beneficial to the FWI (Bunks et al., 1995).

For FWI, the data are also corrected for the discrepancy between the 2-D waveform modeling and the 3-D wave propagation in the real earth. The correction includes a multiplication with $\sqrt{t}$ to compensate for the geometrical spreading effect and a convolution with $1 / \sqrt{t}$ to adjust the phase (Pica et al., 1990). An additional correction is applied on the vertical geophone data to account for the different responses of the hydrophone and vertical geophone sensors. We first invert the source signatures that can best fit the two type of data, respectively, and then compute a filter that transforms the vertical geophone data signature to the hydrophone data signature. Finally, minimum-phase band-pass filter is applied to further denoise and select data for multi-scale FWI.

We only analyze OBS data from the deep-water environment (>1.5 km depth, Figure 2), because the recorded data on the remaining OBSs located on the shallow slope and continental shelf show strong water reverberations that interfere with the primary arrivals and prevent the effective extractions and corrections of shot signatures. These deep-water data were collected using two shooting passes with respective OBS deployments. The two shot segments of the profile roughly connect at 195 km distance (Figure 2). Airgun shots for the profile segment at distances <195 km were of much poorer consistency and quality as indicated by the poor raypath coverage in

Figure 2c. Thus, in the following sections, we use data from both shot segments to perform FAT, but only the data from the shot segment at distances >195 km for FWI.

3.2. First-Arrival Traveltime Tomography

We perform FAT to derive the long-wavelength P-wave velocity model. The data are corrected for OBS locations and shot signatures as described above, and then band-pass filtered within 4.5–12 Hz for enhancing signal-to-noise ratios (Figure 3). We pick 21,290 first arrivals from 63 OBS gathers. An empirically estimated picking uncertainty of 30 ms is assigned to all picks, which is the root sum square of the uncertainties associated with the errors in shot and receiver locations (5 ms, according to the OBS relocation results), the errors in the raypath calculation (16 ms) and the errors in the arrival time picking (25 ms). We perform a least squares tomographic inversion using the code developed by Van Avendonk et al. (2004) and parallelized by Jian et al. (2016). For the ray tracing, a shortest-path method (Moser, 1991) is applied on a graphic grid discretized at 125 m horizontally and 50 m vertically. The inversion model has a sparser grid with 1 km horizontal and 200 m vertical spacing. The starting model is constructed by hanging a best-fitting 1-D velocity profile below the seafloor, which is obtained iteratively prior to the final inversion for the 2-D model. The final 2-D inversion converges after 13 iterations, with smoothing constraints gradually weakened to allow for more model details at later iterations. The inverted model is shown in Figure 2b and Figure 2c shows the ray coverage of the first arrivals. The RMS residual for the starting model is about 280 ms but reduces to about 32 ms after the inversion (Figure 2d), which is close to the picking uncertainty, suggesting a good fit to the data.

The data coverage at distance <195 km is sparse (Figure 2c), because of the poor-quality airgun shots that prohibit effective picking at large offsets. In contrast, the model at distance >195 km is better constrained. The FAT model represents a minimum-structure model, which fits first-arrival traveltimes with overall errors less than half the dominant period of the useful seismic signal (e.g., 133 ms for 7.5 Hz).

3.3. Full Waveform Inversion

3.3.1. Theory

FWI is a powerful technique that utilizes all the information present in seismic waveforms to constrain subsurface models (Tarantola, 1988). In this study, we use the algorithm that was initially developed by Shipp and Singh (2002) to apply 2-D time-domain elastic FWI on dense seismic data with regular acquisition geometry. The code is adapted to accommodate arbitrary acquisition geometries and improve computational performance. We briefly review some key elements of the theory used in our inversion procedure in this section and then discuss some computational considerations for the application on crustal-scale seismic data inversion in the following section.

The wave propagation is modeled by solving 2-D isotropic elastic wave equations using a fourth-order finite-difference method in the time domain (Levander, 1988). The modeled waveform data $d_s^{\mathrm{syn}}\left(M, x_r, t\right)$ from the current model (M) is compared to observation data $d_s^{\mathrm{obs}}\left(x_r, t\right)$ at the receiver locations (x_r). We use a least squares (L^2) misfit function to measure the data misfit:

$$L^2\left(M\right) = \sum_s \int\int \left| w_s\left(x_r, t\right) \Delta d_s\left(M, x_r, t\right) \right|^2 dt dx_r, \tag{1}$$

$$\Delta d_s\left(M, x_r, t\right) = d_s^{\mathrm{syn}}\left(M, x_r, t\right) - d_s^{\mathrm{obs}}\left(x_r, t\right), \tag{2}$$

where $\Delta d_s\left(M, x_r, t\right)$ represents the point-by-point waveform difference, whose L^2 norm is integrated along time (t), receiver locations (x_r), and sources (s) to form the misfit function. The $w_s(x_r,t)$ is a weighting function that can imply data preconditioning like time and offset windowing.

Because of the large computational cost of waveform modeling, one of the keys in the FWI implementation is to efficiently search the extensive model space. The most widely adopted method is the gradient-based search using the adjoint-state method (Lailly, 1983; Tarantola, 1984), which assumes a local linearization of the misfit

function with respect to the model parameters. The model is updated iteratively based on the first-order gradient of the misfit function. At each iteration, the forward-propagating source wavefield ($\vec{u}$) is first calculated, as well as the data residual at receivers (Equation 2), which is then back-propagated simultaneously from all the receivers to generate the adjoint wavefield ($\vec{\varphi}$) (Shipp & Singh, 2002). The gradient of the misfit function with respect to model parameters is efficiently calculated through the cross correlation of these two wavefields:

$$\boldsymbol{g} = \sum_{s} \int_0^T \left(\vec{u} \cdot \vec{\varphi}\right) dt \tag{3}$$

where T is the maximum modeling time and s indicates the summation through all sources. The gradient is further conditioned using a conjugate-gradient method to avoid repeating previous search directions (Fletcher & Reeves, 1964). Finally, a linear estimate method (Mora, 1987; Tarantola, 1984) is used to determine the step length for model update. This requires extra waveform modeling to compute synthetic data from a test model that is derived by perturbing the current model by a small amount along the search direction.

3.3.2. Practical Considerations

The accuracy and efficiency of the waveform modeling are critical for successful application of the FWI. The elasticity is necessary to model the AVO variations when strong contrasts in shear-wave velocities exist (Arnulf et al., 2014; Barnes & Charara, 2009) or multicomponent seismic data are involved. The time-domain modeling allows direct application of time windows on the observed and modeled data. The computational cost of waveform modeling is proportional to the number of sources, but is independent of the number of receivers. In the OBS experiment, the number of airgun shots is tens of times greater than the number of receivers. Thus, it is worthwhile to apply reciprocity to switch the sources and receivers in the modeling. For hydrophone data, both source and receiver are linked to pressure, so the reciprocity simply requires the exchange of their locations. However, for the vertical geophone data modeling, a vertical force is implemented at the OBS location and pressure is recorded at the airgun shot locations. In order to balance the amplitude of pressure wavefield excited by these two different types of sources, we run modeling tests with the FAT model and find that the amplitude of the source function needs to be scaled by 0.4 for the implementation as a vertical force.

One of the difficulties in applications of FWI to crustal-scale studies are the large model dimensions that put high demand on computational resources. It is straightforward to apply parallel programming to multisource time-domain FWI as shot gathers are modeled independently. In order to further improve the computational efficiency, we also implement an expanding box strategy (Shipp & Singh, 2002). Instead of solving the wave equation throughout the model, this strategy first determines a dynamic window in space that outlines the wavefront and then solves the wave equation only within that window. This strategy is particularly effective for the inversion of wide-angle seismic data because the wavefront does not reach the lateral model boundaries until the last time steps. We use rectangular space windows that result in a computational acceleration rate of about 30%.

The computation of gradient requires cross-correlation between the source and adjoint wavefields. This is not straightforward to implement in the time-domain FWI because the source and adjoint wavefields are forward propagated from initial conditions and backward propagated from final conditions, respectively. In this study, we reconstruct the source wavefield by backward propagating from the final source wavefield snapshot at the same pace as for the adjoint wavefield modeling. This method requires to record the source wavefield history only at model boundaries (Shipp & Singh, 2002). However, the memory requirement is still highly demanding in crustal-scale FWI applications. To alleviate the memory burden, we adopt the decimation strategy proposed by Yang et al. (2016), which is based on the fact that the time interval required to sample the wavefield history as defined by the Nyquist theorem is much larger than what is required for waveform modeling. We record the model boundary wavefield at every fifth time step (i.e., resample the wavefield with a time interval of 9 ms) during the forward modeling of the source wavefield, and use a Kaiser-windowed-sinc-function interpolation method (Hicks, 2002) to fill all time steps during the reconstruction. Synthetic tests with the FAT model indicate that the decimation strategy introduces about 0.1% errors that are randomly distributed in the reconstructed wavefield.

3.3.3. Model Setup

The wide-angle arrivals in hydrophone and vertical geophone data contain mainly P-wave energy that does not provide constraints on the long-wavelength Vs or density structures. In order to perform elastic waveform modeling and inversion, Vs and density models are linked to Vp using the empirical relations of Brocher (2005), for

the starting model and during the inversion. Only Vp is actively updated in the FWI. The maximum frequency in the input OBS data is less than 12 Hz. We choose a grid spacing of 25 m to avoid numerical dispersion for P waves. The FAT model (Figure 2b) is interpolated and used as the starting Vp model in the FWI. The time step is 1.8 ms that allows stable wavefield modeling for velocities up to 8.4 km/s.

In the FWI, we only use data from the airgun shots at model distance >195 km, recorded by 47 OBS instruments whose locations are marked as triangles in Figure 2. The full FWI model dimension is 214 × 25 km, consisting of 8561 × 1001 grid points. The maximum offsets with seismic signals are much smaller than the full model dimension. Thus, OBS gathers are accordingly windowed in the spatial dimension to exclude very long-offset traces that are too noisy and do not exhibit coherent seismic signals. In the FWI, the modeling of individual OBS gathers is performed in local windows and the calculated gradient is then copied back to the full model and summed up.

3.3.4. Gradient Preconditioning

The gradient represents the direction of the velocity model update. It is easily contaminated by high-wavenumber artifacts due to the nature of waveform inversion, and by acquisition footprints due to data sparsity and uneven illumination. Thus, preconditioning is required to remove artifacts, enhance low-wavenumber components, convey a priori information, and speed up convergence. In our FWI implementation, a first group of gradient preconditioning rules are applied in the local dynamic window for an individual OBS gather, which includes muting the water column, tapering in the vicinity of the modeling source (i.e., the modeled OBS in this case), and scaling with depth. This preconditioning partially alleviates the issues that arise from lacking a second-order gradient (the Hessian). After the full-model gradient is constructed, a second group of preconditioning rules is applied, which includes the application of a conjugate-gradient method (Fletcher & Reeves, 1964) to speed up convergence, as well as a smoothing regularization.

Although our OBS experiment has a dense instrument distribution in comparison with many other OBS experiments, the data are still sparse in terms of FWI implementations because the OBS spacing is larger than the dominant seismic wavelength (Brenders & Pratt, 2007). Therefore, smoothing regularization is needed to suppress artifacts arising from the data sparseness. As the starting model is a minimum-structure model, it is adequate to ensure the smoothness of output models by directly smoothing the gradient. We apply low-pass filters on the gradient in the wavenumber domain. Two designs of 2-D filters are considered:

$$\left(\frac{k_x^2}{k_{c_x}^2}+\frac{k_z^2}{k_{c_z}^2}\right)^{1/2}=1; \tag{4}$$

$$\left|\frac{k_x}{k_{c_x}}\right|+\left|\frac{k_z}{k_{c_z}}\right|=1, \tag{5}$$

where k_{c_x} and k_{c_z} are the cutoff wavenumbers (wavenumber is defined as the inverse of wavelength throughout this paper) along the horizontal and vertical axis, respectively. Equations 4 and 5 define an ellipse and a rhombus in the wavenumber domain, respectively. While they represent the high-cut boundaries, the low-pass boundaries are correspondingly defined by replacing the value of 1 with 0.5 on the right side of these equations. Between those boundaries, cosine tapers are applied to reduce ringing effects.

Theoretically, the maximum model wavenumber that can be recovered is about twice that of the seismic wavenumber, but this is not achieved unless the data illumination is adequately dense and even (Mora, 1989; R.-S. Wu & Toksöz, 1987). For the sparse OBS data, we choose the cutoff wavenumber by trial-and-error. Figures 5a and 5b show the raw full-model gradient for the first iteration, in the space and wavenumber domain, respectively. The maximum $|k_x|$ along the horizontal axis is about 0.3 km^{-1}, whereas the maximum $|k_z|$ along the vertical axis is about 1.5 km^{-1}. The maximum $|k_z|$ value corresponds to the theoretical limit, assuming a seismic wavelength of about 1 km and a scattering angle of about 45° (see Sirgue & Pratt, 2004, for theoretical derivation). After extensive tests, we set k_{c_z} as 1.667 km^{-1} (corresponding to model wavelength of 600 m) for the FWI of wide-angle OBS data. On the other hand, the maximum $|k_x|$ along the horizontal axis is much smaller because of the intrinsic limitation of wide-angle surface data acquisition, the lateral homogeneity of the heavily sedimented continental margin, and the sparsely distributed OBS instrumentation. The OBS spacing varies from <3 km to >10 km, but

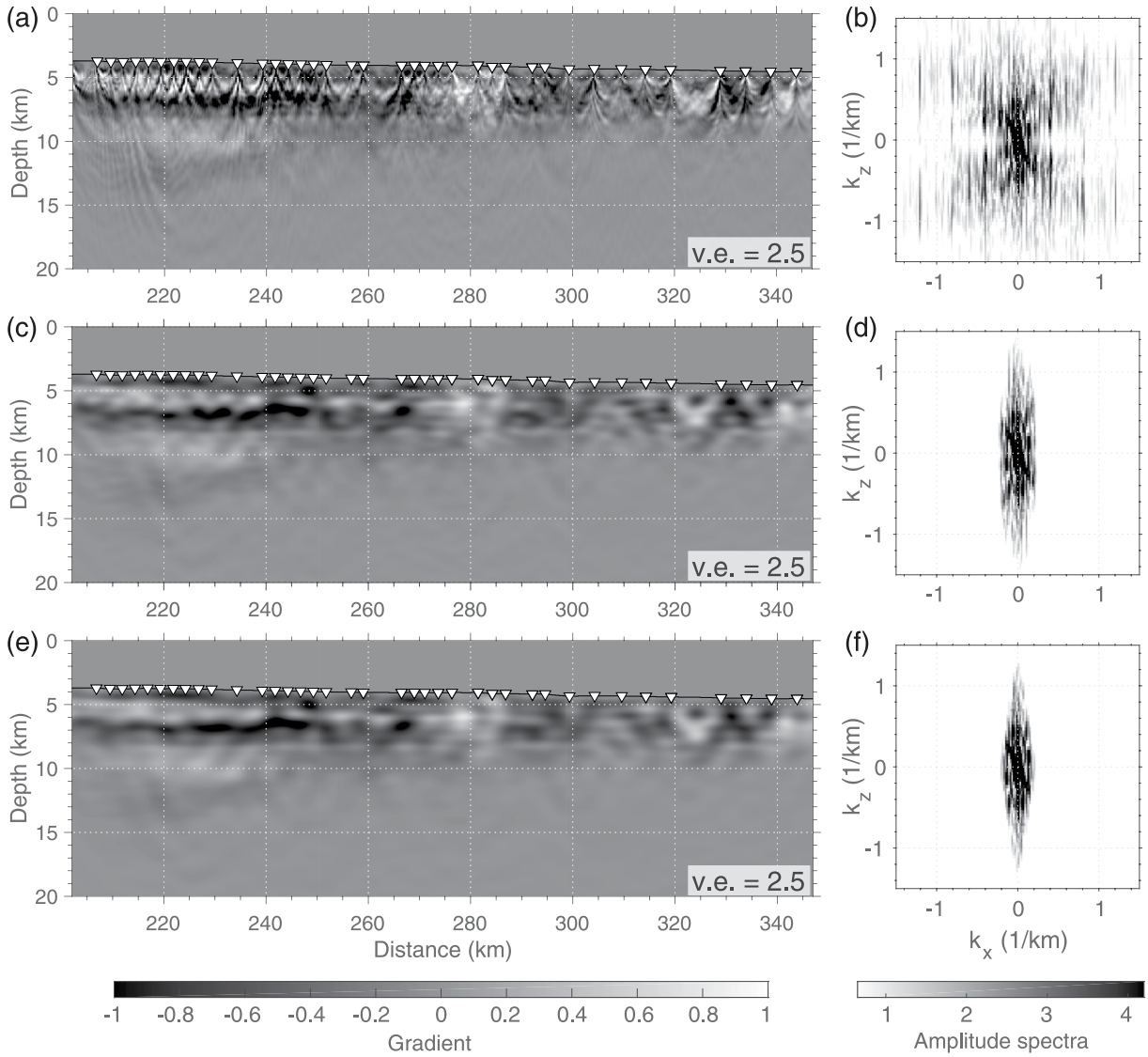

Figure 5. Comparison of wavenumber-domain filters applied to the initial gradient in the OBS FWI. Spatial image (a) and wavenumber-domain amplitude spectrum (b) of the raw gradient after muting the water column. (c) and (d) are the space- and wavenumber-domain plots of the gradient after filtering using the ellipse-shaped 2-D filter (Equation 4). (e) and (f) are similar to (c) and (d), except for use of the rhombus-shaped 2-D filter (Equation 5). White triangles mark OBS locations. The acquisition footprint associated with sparse data coverage is observed in the raw gradient as dipping features in the space domain and periodic amplitude peaks expanding along diagonal lines in the wavenumber domain. Better suppression of the acquisition footprint is achieved by the rhombus-shaped 2-D wavenumber filter.

for most of the profile it does not exceed 4–5 km. Thus, we heuristically set k_{c_x} as 0.25 km^{-1} for a balance between model resolution and acquisition footprint removal.

The diagonal area in the wavenumber-domain plot (Figure 5b) exhibits periodic amplitude peaks that largely exceed the maximum $|k_x|$ observed on the horizontal axis. Those diagonal peaks correspond to the dipping features at shallow depths in the space domain (Figure 5a), which are associated with the sparse OBS distribution, representing acquisition footprints. Figures 5c–5f compare the effects of the two low-pass filters, with an ellipse shape (Equation 4) and a rhombus shape (Equation 5), respectively. With the same on-axis cut-off wavenumber values as described above, the rhombus-shaped filter result is more satisfactory, as it suppresses artifacts better while not degrading model information. In conclusion, for gradient smoothing in the OBS FWI, we use the rhombus-shaped low-pass wavenumber filter (Equation 5), with the cut-off wavenumber: $k_{c_x} = 0.25\,\mathrm{km}^{-1}$ and $k_{c_z} = 1.667\mathrm{km}^{-1}$.

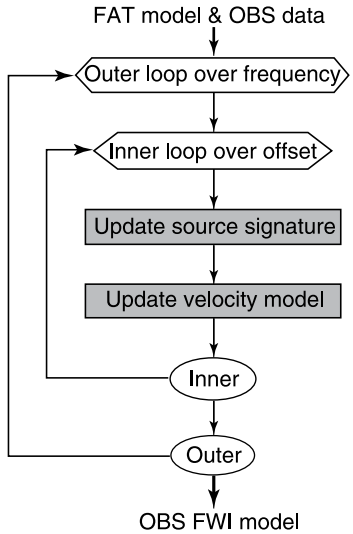

Figure 6. The ocean bottom seismometer full waveform inversion workflow, including two loops over frequency bands and time-offset windows, respectively. The outer loop contains two options for the frequency band: 3.5–6.5 Hz and 3.5–10 Hz. The inner loop over time-offset windows also contains two options: (1) the middle and long-offset wide-angle phases (black and cyan curves in Figure 3) and (2) only long-offset early arrivals (black and blue curves in Figure 3).

3.3.5. Data Preconditioning and Inversion Scheme

Time and offset windows are readily implemented in the time-domain modeling approach to precondition seismic data (Equation 1). Throughout the OBS FWI, we exclude traces with less than 3 km offset (e.g., Figure 3) in all OBS gathers for two reasons. First, the shooting profile is crooked, which has strongest effect on the near-offset early arrivals because of their short travel distance (Kamei et al., 2015). We exclude the near-offset traces to alleviate the crooked-line effect. Second, the near-offset traces are dominated by sub-vertical reflections that are sensitive to short-wavelength model structures and create strong high-wavenumber components in the FWI gradient (Sirgue & Pratt, 2004). Incorporation of sub-vertical reflections at the early stage of FWI would hinder the convergence to the global minimum, unless some hierarchical modeling and inversion strategies, like reflection FWI (Xu et al., 2012) are applied. On the other hand, the sub-vertical reflections may be inverted at the later stage of FWI. However, the sparseness of the OBS data requires smoothing regularization that impedes the fitting to sub-vertical reflections. In conclusion, we exclude those near-offset traces and focus on recovering the long- and medium-wavelength velocity models.

We design two data windows for the OBS FWI. One is a long-offset early arrival window starting at 100 ms prior to the first arrival (black curves in Figure 3). The length of the time window is laterally variable so that direct waves are excluded, up to a maximum length of 1.6 s (blue curves in Figure 3). This window naturally excludes traces with offset less than about 9.5 km. The other one is a middle to long-offset window (black and dashed cyan curves in Figure 3) that extends the long-offset window to include middle-offset (between ~9.5 and 3 km) arrivals, such as shallow diving waves and critical-angle reflections from shallow boundaries. In the inversion scheme (Figure 6), we first use the middle to long-offset data window because these data better constrain the sedimentary layers. Then, a FWI with the long-offset data window is performed to focus on fitting weak long-offset arrivals that constrain the model at larger depths.

For the P-wave velocity inversion, we use vertical and hydrophone data that are dominated by compressional wave energy. Figures 3e and 3f compare processed vertical and hydrophone channel records from OBS 59. They are very similar in long-offset early arrivals, whereas the vertical channel records have better signal-to-noise ratios, especially at offset over 20 km. In contrast, after the direct water arrivals, near-offset and critical-angle P-wave phases from shallow sedimentary layers can be easily identified on the hydrophone channel record, but are largely obscured on the vertical channel record. These differences are observed on all OBS gathers, suggesting that different data preconditioning needs to be applied on the two channels. In conclusion, when utilizing the middle to long-offset data window, we use only hydrophone channel data. On the other hand, when applying the long-offset data window, we use vertical channel data wherever it successfully recorded seismic signals (Figure 2a), otherwise use hydrophone data.

In addition to the offset-continuation strategy implemented through time-offset windows, the data are also preconditioned following a frequency-continuation strategy (Bunks et al., 1995). The lowest signal frequency available in the OBS data is about 3.5 Hz, although the signal-to-noise ratio is quite low below 4.5 Hz. The inversion starts from using low-frequency data between 3.5 and 6.5 Hz and then proceeds to use wide-frequency data between 3.5 and 10 Hz. To combine these two strategies, we put the loop over time-offset windows inside the loop over frequencies (Figure 6), but we speculate that the opposite way can work equally well. The final data preconditioning is a mild offset weighting of the L^2 misfit function (Equation 1) that scales traces with the absolute values of their offset to the power of 0.25. This scaling is applied in all inversion steps.

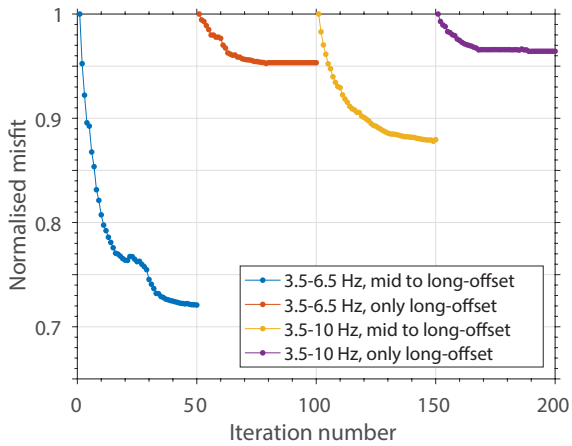

Figure 7. Evolution of the overall misfit in the ocean bottom seismometer full waveform inversion. Following the inversion scheme (Figure 6), four steps are performed with different data preconditioning that loop over two choices of time-offset windows and two choices of frequency bands. In each step, 50 iterations are run. The final model in a step serves as the starting model in the following step.

4. Results

4.1. Full Waveform Inversion Results

Following the inversion scheme described above (Figure 6), four steps of OBS FWI are performed with different data preconditioning that loop over two time-offset windows and two frequency bands. Each step is completed with 50 iterations. Figure 7 shows the evolution of overall data misfit. A relatively larger misfit reduction is achieved at the first and third steps where new frequency components are added. On the other hand, the reduction is smaller in the second and fourth steps with data windows shrinking, because the data that need to be fitted have been included in the previous steps. Figure 8 demonstrates the data fitting for early arrivals recorded by OBS 59. The initial modeled data from the FAT model show good fit to the travel time of first arrivals with time delays less than half of the dominant seismic periods for most traces (Figure 8c). The phase difference (Figures 8g and 8h) between the initial modeled and observation data shows only few values lying outside $[-\pi, \pi]$ that is indicative of cycle skipping, justifying the use of the FAT model as the starting model for FWI. However, the triplications and secondary arrivals are not well fitted by the FAT model, for example, the triplications around $\pm$11 and $-$28 km offset (Figures 8a, 8c, and 8e). After the FWI, they are better fitted (Figures 8d and 8f), due to the negative velocity update around 6–7 km depth and 11–14 km depths, respectively (Figure 8b). Additional examples for the data fitting are presented in Figures S1–S5 in Supporting Information S1.

Figure 9 displays the inverted velocity models at the end of the second and fourth steps, respectively, which correspond to iteration numbers of 100 and 200 in Figure 7. The model update relative to the starting model is displayed in Figure S6 in Supporting Information S1. Figure 10 presents the gradient of the final OBS FWI model (Figure 9b) that highlights the fine-scale variations revealed by the FWI.

4.2. Resolution Tests

We conduct resolution tests for the OBS FWI. The procedure includes several steps. First, we build input models by adding checkerboard perturbations with different size, to the OBS FWI model (Figure 9b) below the seafloor. Second, synthetic seismic data are generated from the input models using the same acquisition geometry as for the field data. Third, we add noise to the synthetic data. In order to mimic the noise in the field data, we create Gaussian noise gathers with the same size as the OBS data gathers, and band-pass (3.5–10 Hz) filter them. The filtered noise's amplitude is independent of offset, and the overall amplitude is tuned so that the RMS energy of the noise gather is half of the RMS energy of the windowed arrivals in the corresponding synthetic OBS gather. The composite noisy data gathers have good signal-to-noise ratios at near offsets and very noisy traces at the furthest offsets where we have picked first arrivals, similar to what is observed in the field data (Figure S7 in Supporting Information S1). Finally, the noisy synthetic data are inverted, starting from the unperturbed model (i.e., the OBS FWI model), to recover the perturbations. Unlike the field data inversion, this inversion is simplified to complete in one step, using the same data and gradient preconditioning as in the last step of the field data inversion (long-offset data window and frequency band between 3.5 and 10 Hz). This approach is valid because the high-wavenumber checkerboard perturbations do not pose cycle-skipping problems for the FWI of wide-frequency data.

Figure 11 shows recovered perturbations from two checkerboard tests with different spatial dimensions of (I) 6 $\times$ 1.5 km and (II) 4 $\times$ 1 km. The horizontal $\times$ vertical dimension format is used throughout the paper. The checkerboard pattern I is recovered excellently throughout the model area covered by first-arrival ray paths (Figure 11a). The result of checkerboard test II (Figure 11b) discloses the uneven illumination. At distance <280 km, the perturbations are recovered excellently at most depths. At distance >280 km, the perturbations are well

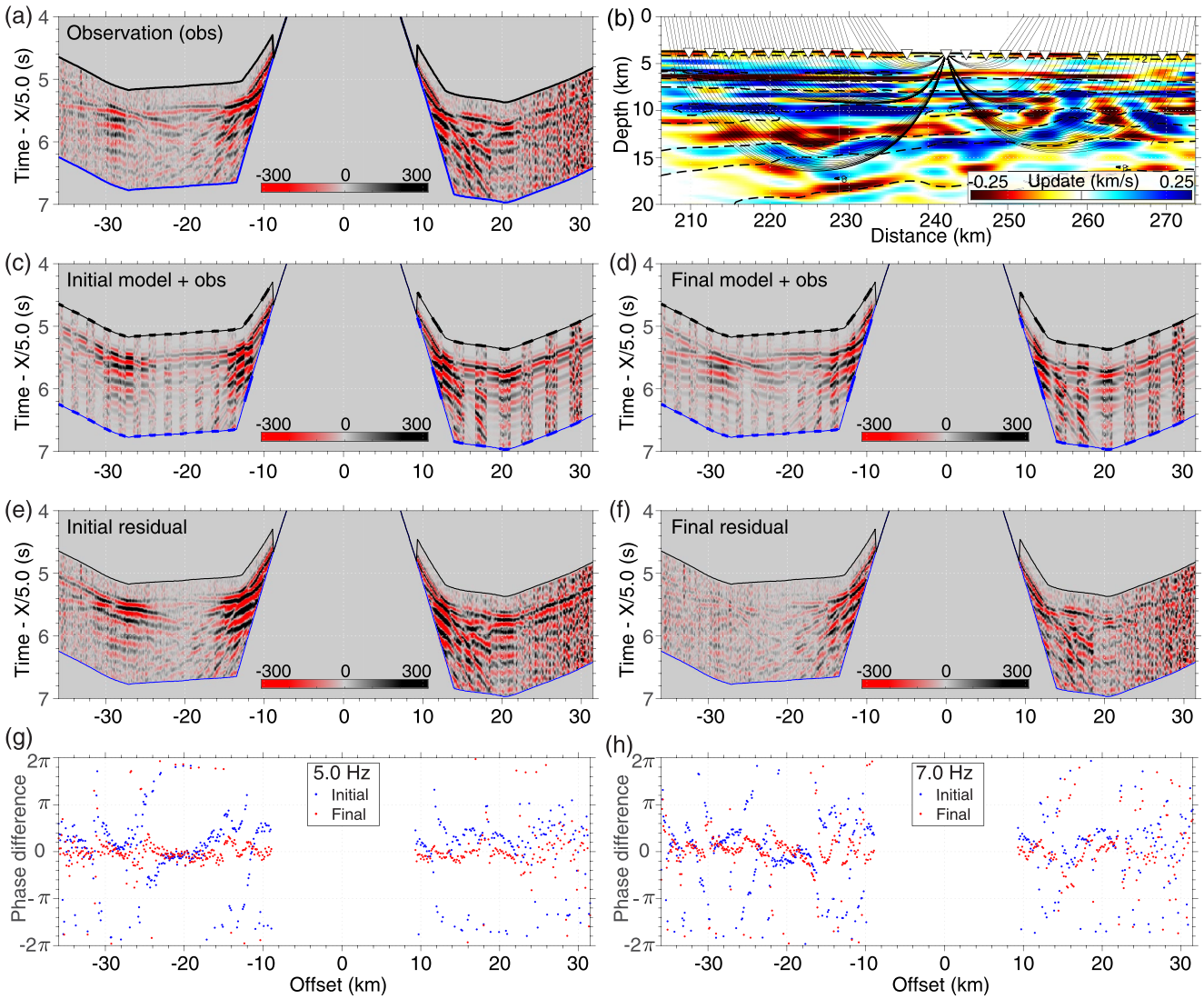

Figure 8. Example of data fitting for long-offset early arrivals in the vertical geophone record of OBS 59. (a) Preprocessed observation data after mute using the long-offset time-offset window. Black and blue curves represent the top and bottom muting locations, respectively. (b) Ray paths for first arrivals overlying the ocean bottom seismometer (OBS) full waveform inversion (FWI) model update (Figure S6c in Supporting Information S1), where dashed curves represent velocity contours spaced at every 1 km/s corresponding to the OBS FWI model (Figure 9b). Triangles mark OBS locations. (c) Initial synthetic data from the first-arrival traveltime tomography model (Figure 2b), interleaved with the observation data in alternative bins of 10 traces. Observation data are bounded by bold black and blue curve segments. (d) Same as (c), but for the final synthetic data from the OBS FWI model (Figure 9b). (e and f) are data residuals for the initial and final synthetic data. (g) Phase difference between observation and initial synthetic data (blue dots), and between observation and final synthetic data (red dots) at 5 Hz. (h) Same as (g), except at 7 Hz.

recovered at shallow depths (<11 km), whereas at large depths the perturbations have correct locations but are smeared out and have reduced amplitudes.

The Vs and density structures are linked to the Vp through an empirical relationship. We run additional inversion tests to assess the effect on the inverted Vp models of the assumed Vs and Vp relationship. The noisy synthetic data generated in checkerboard test I are inverted, using two different Vs-Vp relationships where the Vs is 10% lower or higher than that used in generating the synthetic data. The recovered perturbations of Vp (Figure S8 in Supporting Information S1) show mild distortions in the shape of the positive and negative anomalies, but the locations are correctly recovered.

A model feature of important geological meaning is the Moho transition zone (MTZ). In order to assess the ability of the OBS FWI to resolve a sharp MTZ, we perform a synthetic test. Figure 12a shows the OBS FWI model zoomed in around the potential MTZ depths, where the velocities are smoothly increased from deep

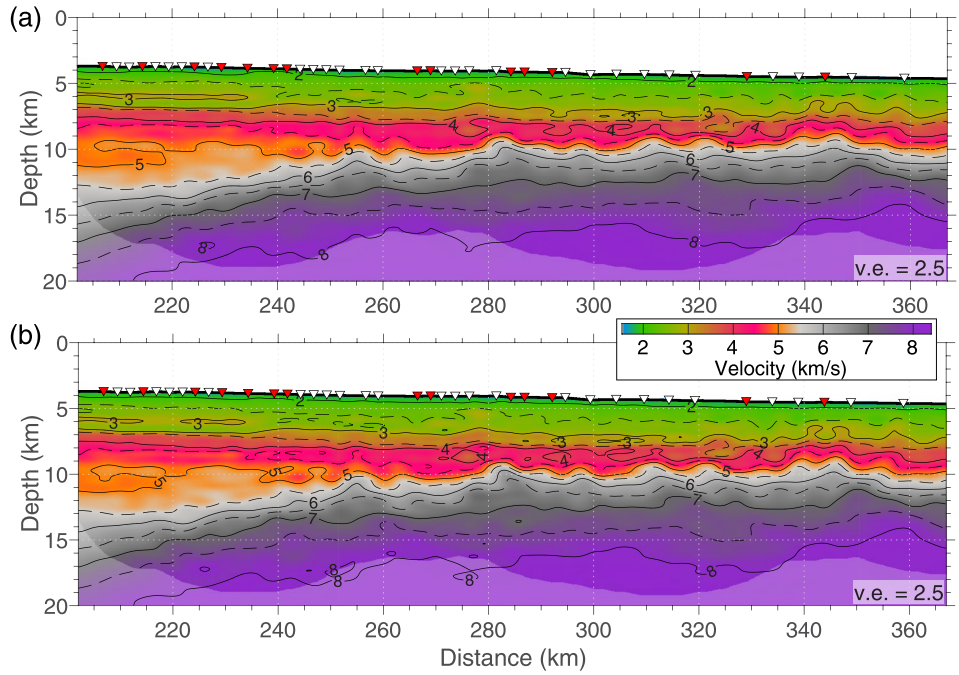

Figure 9. Model results from the ocean bottom seismometer (OBS) full waveform inversion (FWI). (a) The velocity model using low-frequency (3.5–6.5 Hz) OBS data. (b) The velocity model using wide-frequency (3.5–10 Hz) OBS data. The two velocity models (a) and (b) are outputs from iteration number 100 and 200 in Figure 7, respectively. Note that the FWI is performed from model distance 195 km to model distance 408 km, but the data at distance >350 km are too sparse for making detailed interpretations. Inverted triangles are OBS locations. Red color indicates OBSs with good-quality records on both hydrophone and vertical geophone channels, whereas white color indicates OBSs where only hydrophone data are of high quality. Model area that is not covered by the ray paths of first arrivals from the OBS gathers used in the FWI is shaded. The vertical exaggeration is 2.5.

crustal velocities (≤7.2 km/s) to uppermost mantle velocities (≥7.9 km/s). We insert a sharp MTZ to the model around the depth of 7.55 km/s velocity contour, with the velocity increase from 7.2 to 7.9 km/s occurring over 0.5 km depth range (Figure 12b). Above and a below the MTZ, the velocities are high-cut and low-cut at 7.2 and 7.9 km/s, respectively. This model is used to generate synthetic data, to which noise is added. Starting from the unperturbed model (Figure 12a), we perform inversion of the noisy synthetic data in the same way as for the checkerboard tests. The recovered Vp model is shown in Figure 12d. Figures 12c and 12e show the perturbations of the input and recovered models with respect to the starting model, respectively. The results indicate that this sharp MTZ can be well resolved at model distance ≤340 km, whereas the resolvability gradually weakens towards greater model distance.

In summary, the resolution tests demonstrate that the model resolution is as high as 6 × 1.5 km in most model area covered by first-arrival ray paths, while a higher resolution (4 × 1 km) can be resolved at distance <280 km. The synthetic test for MTZ indicates that the OBS FWI is capable of reconstructing a sharp MTZ at model distance ≤340 km. We also test the effect of the assumed Vs-Vp relationships on the inverted Vp model. However, we would like to note that other factors, like anelasticity and 3-D effect, are not considered in our field data inversion and synthetic tests.

4.3. Prestack Depth Migrated Image

Based on the FWI velocity model derived above, we perform Kirchhoff prestack depth migration (PSDM) using the coincident MCS data that cover the model distance <280 km (Figure 1a). The MCS data were acquired and preprocessed by GX Technology Corporation (GXT). The streamer was 9 km-long, containing 360 hydrophone groups spaced at 25 m. The GXT processing includes zero-phasing, noise attenuation, trace editing, and multiple removal. The PSDM image is shown in Figure 13b and Figure S9 in Supporting Information S1. For comparison, the PSDM image that was generated by the GXT company based on the velocity model derived using reflection

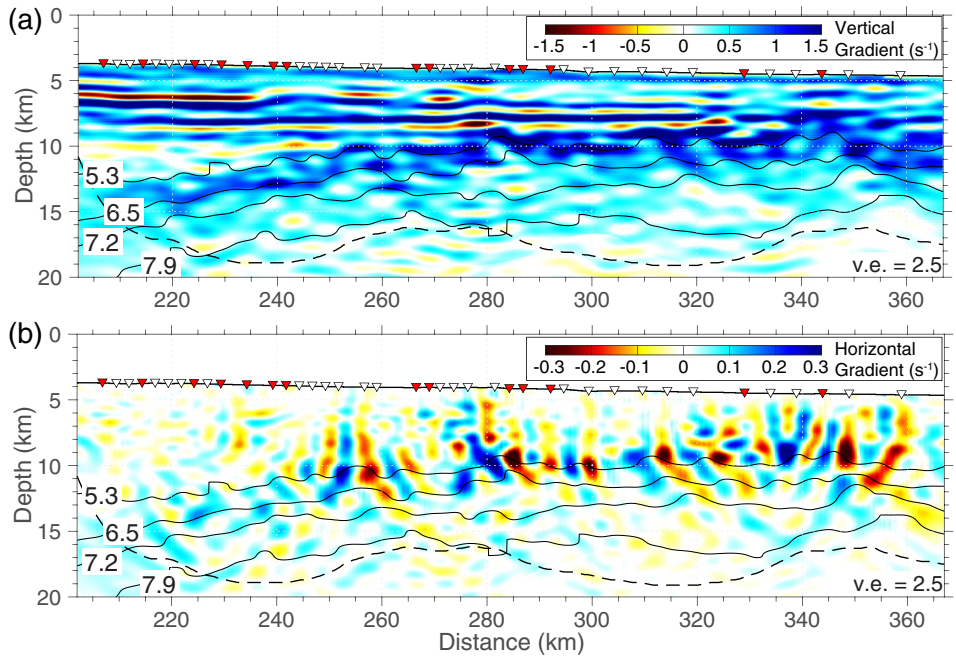

Figure 10. Gradient of the ocean bottom seismometer full waveform inversion (FWI) model (Figure 9b): (a) vertical gradient and (b) horizontal gradient. Note the different color scales. The solid black curves are the velocity contours at 5.3, 6.5, 7.2, and 7.9 km/s. The dashed black curves mark the bottom of model area that is covered by first-arrival ray paths involved in the FWI. The vertical exaggeration is 2.5.

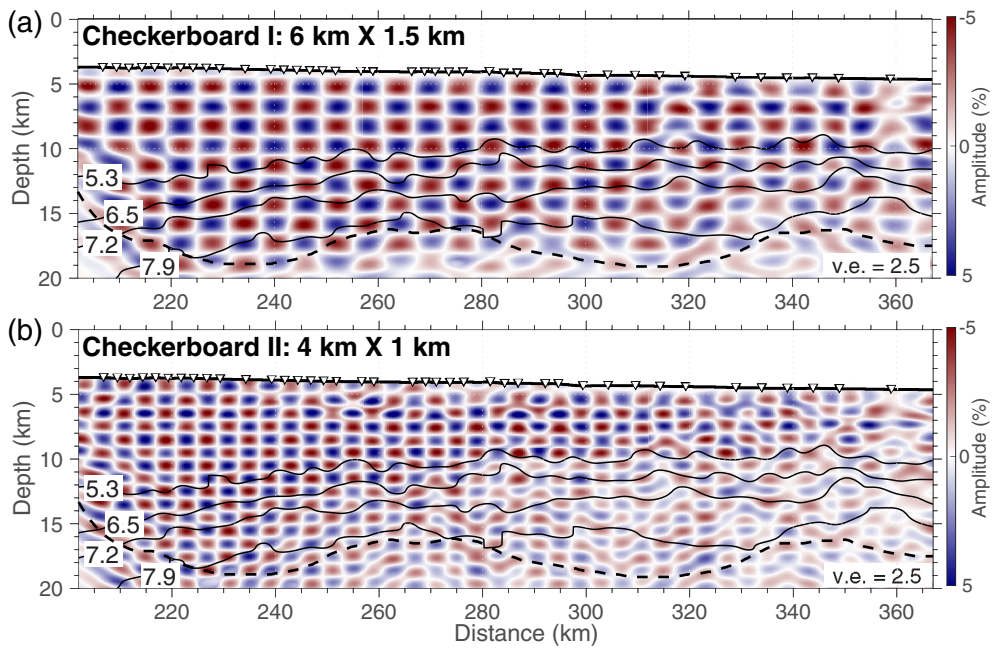

Figure 11. Recovered models from checkerboard tests of the ocean bottom seismometer (OBS) full waveform inversion (FWI), with input perturbation dimensions of (a) 6 × 1.5 km and (b) 4 × 1 km. The maximum values of the input perturbations are 5%. The dashed black curves mark the bottom of areas covered by first-arrival ray paths for the data traces used in the FWI. The solid black curves are velocity contours from the OBS FWI model.

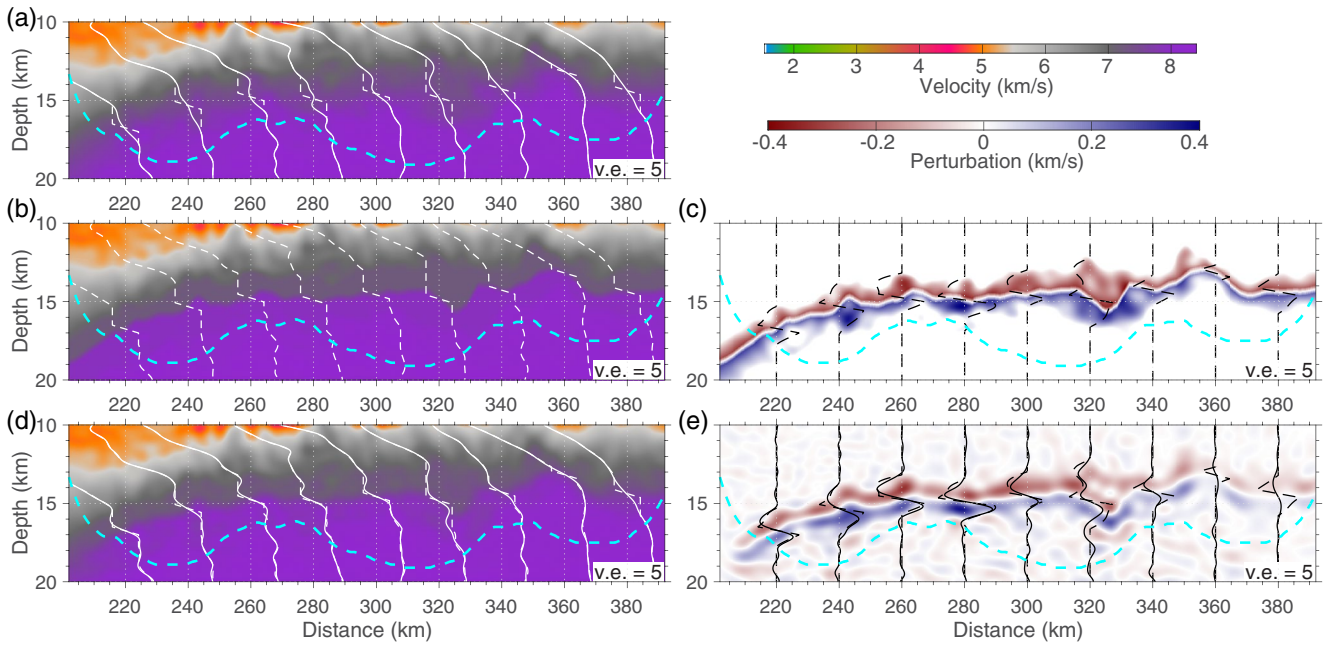

Figure 12. Synthetic test for recovering sharp Moho transitions. (a) The ocean bottom seismometer full waveform inversion (FWI) model (Figure 9b), which is used as the starting model of the synthetic inversion test. (b) The model that is modified from (a), by adding a sharp MTZ from 7.2 km/s to 7.9 km/s in a depth window of 500 m around the 7.55 km/s velocity contour. This model is used to generate noisy synthetic data. (c) Difference between (b) and (a). (d) The recovered model, and (e) its perturbations relative to the starting model (a). In all plots, 1-D profiles are plotted at every 20 km between 220 and 380 km distance, for velocities (white curves) or perturbations (black curves): the dashed curves for the model with the sharp MTZ; and the solid curves for the starting or recovered models. The dashed cyan curves mark the bottom of areas covered by first-arrival ray paths for the data traces used in the FWI.

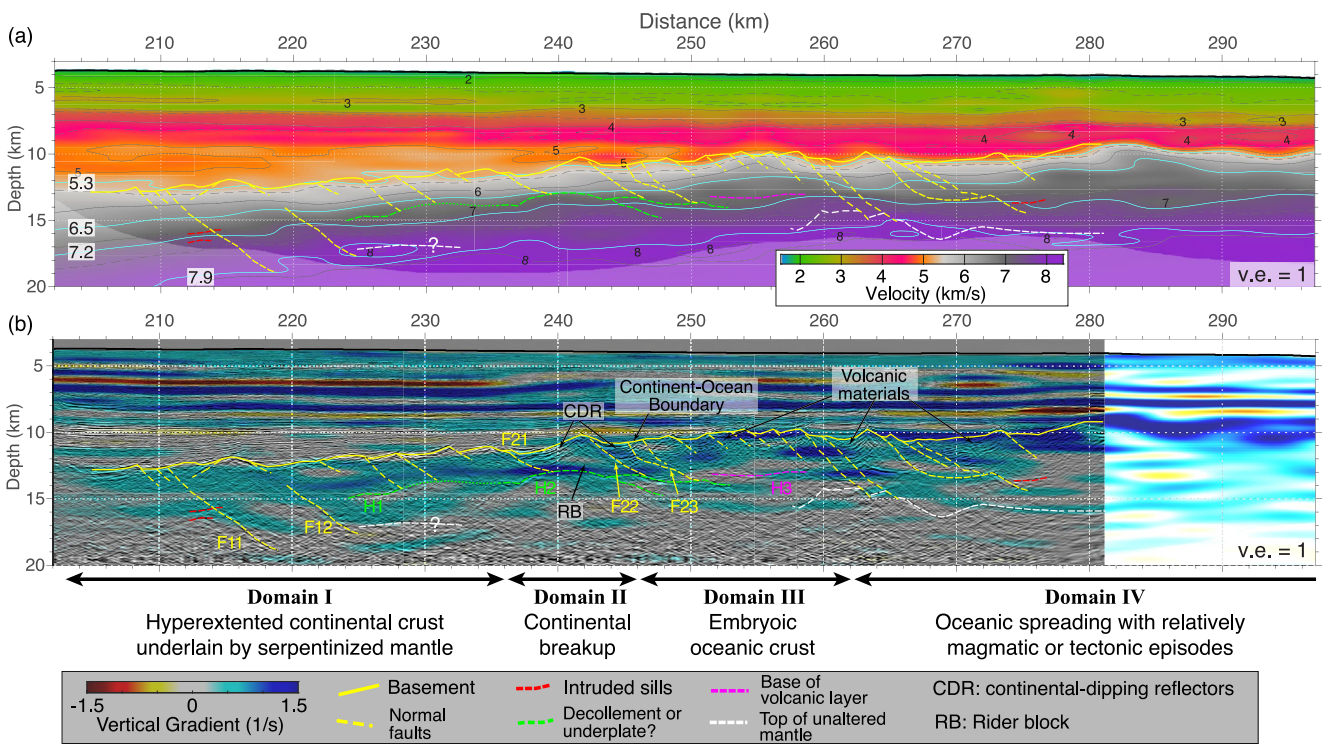

Figure 13. Comparison of the full waveform inversion (FWI) (a) velocity model and (b) the PSDM reflection image. The gray-scale reflection image in (b) is underlain by the vertical gradient of the FWI model (Figure 10a) shown in blue and red colors. Interpretations are drawn on the reflection image and copied to the velocity model plot. Solid and dashed black curves are velocity contours spaced at 0.5 km/s, with additional contours at 5.3, 6.5, 7.2 and 7.9 km/s (cyan curves).

velocity analysis is shown in Figure S9a in Supporting Information S1. Due to the constraints from the OBS data on the FWI velocity model, our PSDM result shows improved imaging of the top basement and intrabasement reflectors.

4.4. Joint Analysis of Velocity Models and Migrated Image

The model at distance <280 km is best constrained in our results, where the FWI model has the highest resolution (Figure 11) and the PSDM image is available. Our FWI routine aims to retrieve the long- to medium-wavelength background velocity models, whereas the PSDM image contains only sharp layer boundary information. A resolution gap exists between them (Claerbout, 1985). To highlight the finer-scale features added by the FWI, we take into account the FWI model gradient and plot it together with the PSDM reflection image (Figure 13b). We also manually pick seismic reflections in the crystalline basement from the PSDM image (Figure 13b and Figure S9c in Supporting Information S1) and plot them over the FWI model for comparison (Figure 13a). Although the FWI model is derived without any input from the MCS data, its consistency with the image is remarkable. For example, the strong vertical gradients within the sedimentary layer are well correlated with imaged reflectors. In this section, we focus on analyzing the correlation between velocity models and the reflection image from the basement top to the mantle.

4.4.1. Basement Top

The velocity variations around the basement top are highly consistent with the PSDM image, up to a resolution of 4 × 1 km as demonstrated by the FWI resolution tests. The imaged basement top reflector coincides well with the top of the high-gradient basement layer in the FWI model (Figure 13b). In Figure 14, we compare velocity-depth profiles extracted from different velocity models (layered, FAT, and FWI) at six locations, three of which within the region of the PSDM image. At distance <240 km (Figure 13a), the lowermost sediment unit has velocities of 5–5.2 km/s, down to depths of >12 km (Figure 14a). Below this sediment unit, the FWI model resolves a small velocity jump and increased vertical velocity gradients below the acoustic basement top reflector that is picked from the PSDM image (black arrow in Figure 14a). This feature is constrained in the OBS data by the triplication feature at ∼20–35 km offsets as shown in Figure 8. In contrast, the FAT and layered models do not recover any velocity jumps across the imaged basement top reflector, possibly due to the lack of turning rays in the thin low-velocity uppermost basement layer (marked with the blue arrow in Figure 14a) (Lau et al., 2018). On the seaward side of 240 km distance, the lowermost sediment unit pinches out, so that no sediment layers have velocities exceeding 5 km/s. The basement is simply identified as a sharp transition of velocities from <5 km/s to >5.5 km/s (Figure 14). Correspondingly, the imaged top basement reflector mostly lies between the 5.0 and 5.5 km/s velocity contours (Figure 13a), indicating an excellent match between the lateral velocity variation and the imaged basement topography. This comparison suggests that we can confidently estimate the basement location from the velocity model at distances >280 km, outside of the region imaged by the MCS data. For simplicity, we choose the velocity contour of 5.3 km/s (C5.3) to represent the top basement boundary. Although the top basement velocity may vary laterally, the sharp vertical velocity transition from 4.5 to 5.5 km/s within hundreds of meters indicates that the error in the depth estimation for this boundary does not exceed 0.5 km, assuming that the velocity model is correct up to a resolution of 4 × 1 km.

4.4.2. Crustal Structure

Within the basement, we pick numerous reflection events that are subhorizontal or dipping seaward. Around 260–264 km distance, there is a rapid seaward velocity drop between the 5.5 km/s to 7.5 km/s velocity contours, across two large dipping reflectors (Figure 13a), suggesting that they are deep-cutting normal faults. These faults can also be recognized from the horizontal gradient of the FWI model as seaward dipping high-gradient belt with alternating negative and positive values (Figure 10b). Other imaged dipping reflectors (yellow dashed curves in Figure 13) are also interpreted as normal faults due to their relationship to the basement morphology, although the correlation with intrabasement velocities is less pronounced. Furthermore, subhorizontal reflectors are widely observed within the basement (red and green curves in Figure 13). They mostly correspond to seismic velocities between 6.5 and 7.2 km/s.

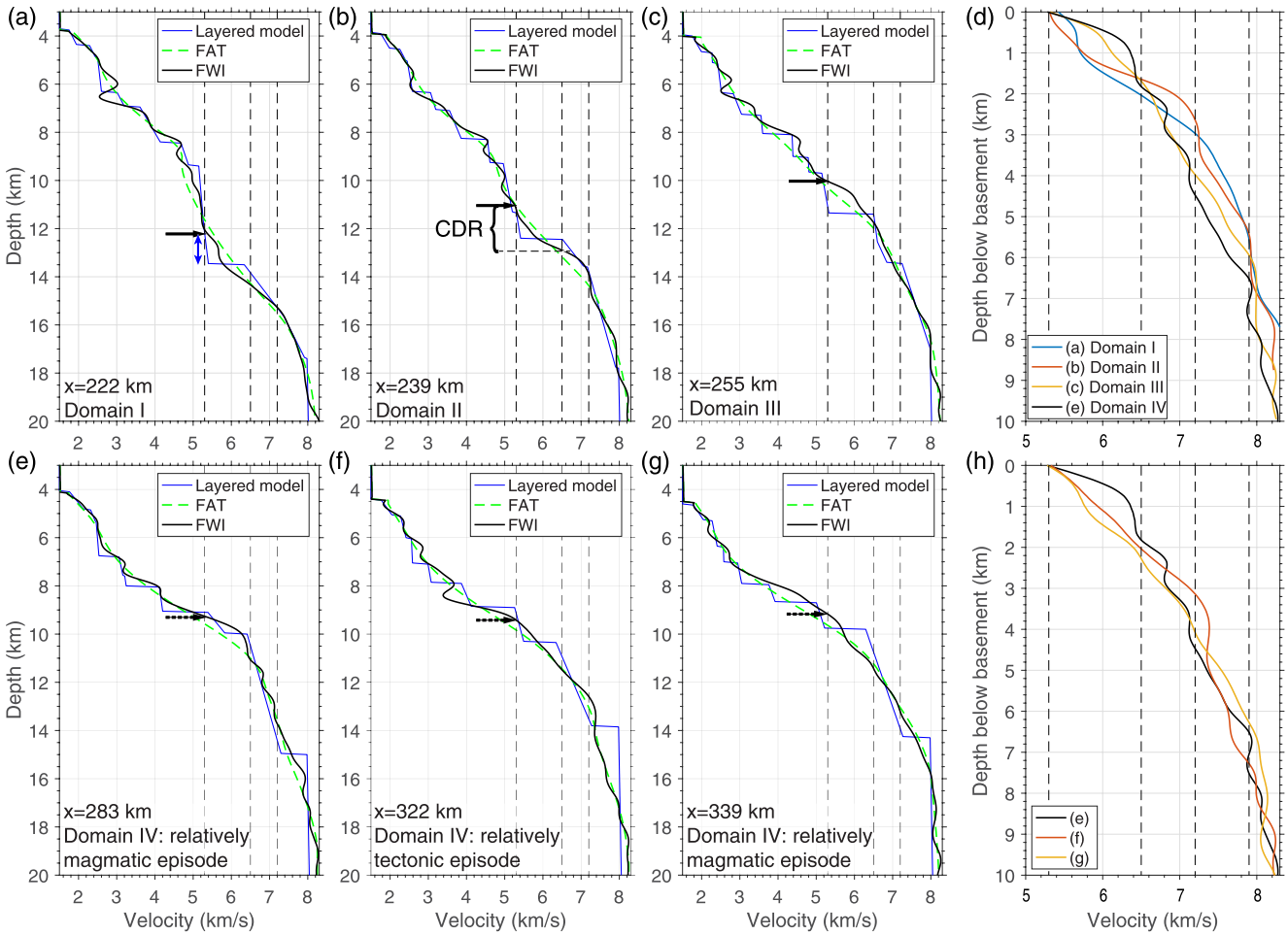

Figure 14. Velocity-depth profiles of the layered model from Lau et al. (2018) (Figure 2a), the first-arrival traveltime tomography model (Figure 2b), and the full waveform inversion model (Figure 9b). Panels (a–c) are extracted from Domain I, II and III, respectively. Panels (e–g) are located at the center of three identified spreading episodes in Domain IV. Vertical dashed lines are grid lines at velocities of 5.3, 6.5 and 7.2 km/s. The blue vertical arrow in (a) marks the thin low-velocity layer at the uppermost part of basement. Black arrows mark the top basement locations picked from the PSDM reflection image (solid arrows) or based on the 5.3 km/s velocity contour (dashed arrows). (d) Comparison of the basement velocity profiles from the four domains (a–c, e), with all profiles aligned at the basement top. (h) Similar to (d), but for profiles extracted at different oceanic spreading episodes (e–g). Velocities of 5.3, 6.5, 7.2, and 7.9 km/s are marked as vertical dashed lines.

The landward edge of our study area lies close to the continental breakup front suggested by Louden et al. (2013) and in the middle of the COT defined by Lau et al. (2018). In order to better understand the nature of the crust, we pay attention to intra-crustal velocity contours at 6.5 km/s (C6.5) and 7.2 km/s (C7.2) (Figures 13a and 15a). These velocity contours generally correspond to the velocities expected at the bottoms of oceanic layers 2 and 3, respectively, in the magmatic oceanic crustal model (Christeson et al., 2019). Although under the magma-poor rifting and slow-spreading scenario the crust is more likely to be composed of mixed igneous rocks and serpentinized mantle (Cannat, 1993) that have overlapping seismic velocities (Miller & Christensen, 1997), analysis of the lateral variations of these velocity contours can still help determine the nature of the rifted and/or accreted crust. Although no velocity discontinuities are observed within the basement, Figure 10a does show a systematic variation of vertical velocity gradients across C6.5 and C7.2, where the gradient is smaller in deeper layers.

4.4.3. Crust/Mantle Transition

At the seaward end of the reflection image (distance between 259 and 281 km), we pick a weak subhorizontal reflector at 14–16 km depth (white dashed curve in Figure 13 and Figure S9c in Supporting Information S1).

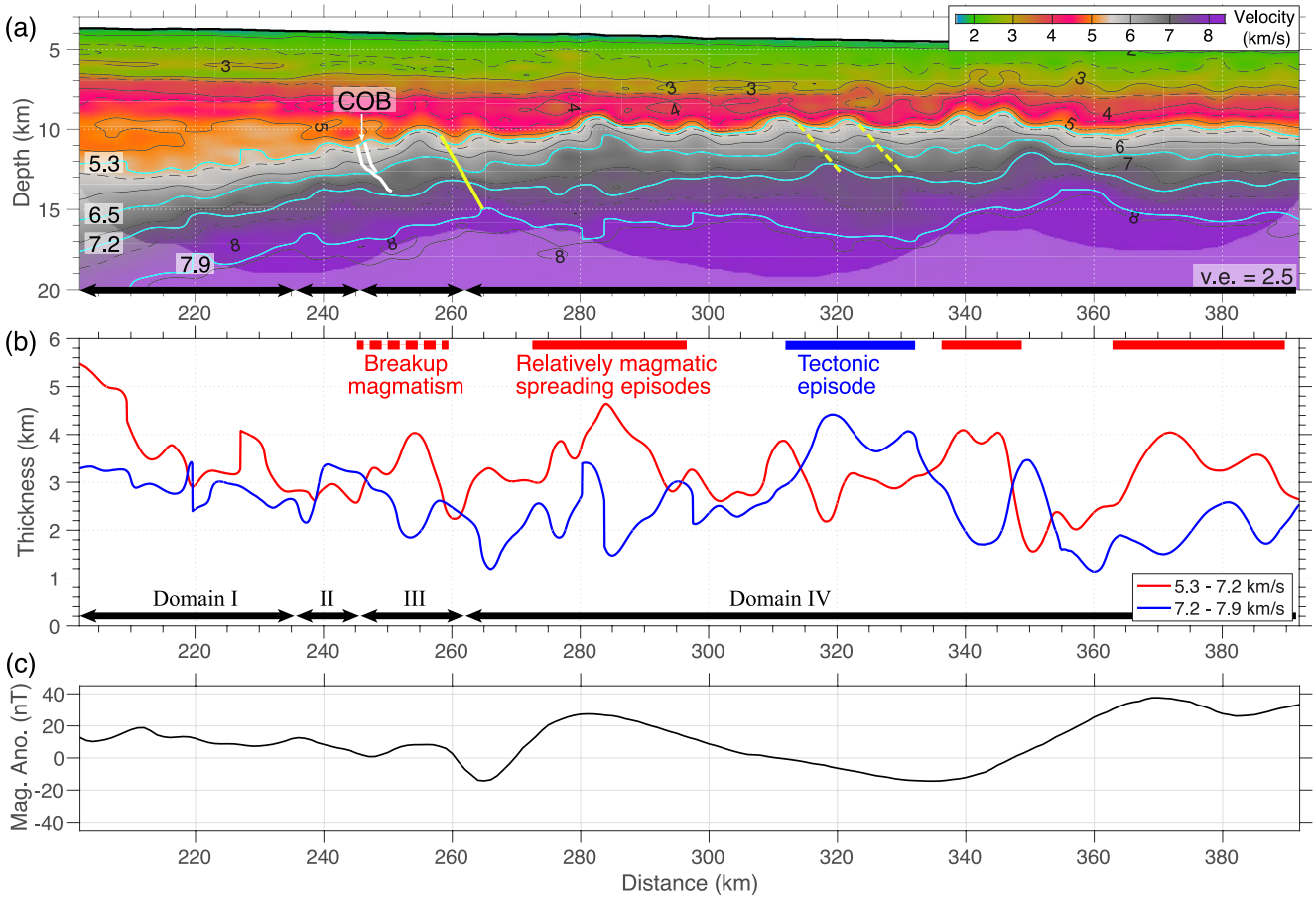

Figure 15. (a) Full waveform inversion (FWI) model. Solid and dashed black curves are velocity contours at every 0.5 km/s, while additional velocity contours of 5.3, 6.5, 7.2, and 7.9 km/s are shown as cyan curves. The solid and dashed yellow lines indicate the large-throw normal faults within the slow-spreading seafloor, picked from the PSDM image and speculated from the FWI velocity model, respectively. The white curves indicate the interpreted continent-ocean boundary (COB). (b) Thickness between the select velocity contours. The red bars on the top indicate the rifting or drifting episodes with relatively more magmatic additions to the crust, and the blue bar marks the more tectonically dominating episode. The black arrows at the bottoms of (a) and (b) mark the four interpreted domains. (c) Magnetic anomaly along the OETR-2009 profile, extracted from the magnetic anomaly map (Figure 1b).

It approximately coincides with the 7.9 km/s velocity contour (C7.9) and is offset by the deep-cutting dipping reflectors around 263 km distance. Around 278 km, it also coincides with a weak increase in vertical velocity gradient at ~16 km depth (Figure 13b), indicating a transition zone around 7.9 km/s. We interpret this reflector as the top of unaltered mantle. The 7.9 km/s velocity is a little lower than typical mantle velocities of 8.0 km/s (Christensen & Mooney, 1995), but the depth differences between these two velocities contours are generally small in our model, especially at a distance >285 km where it is less than 0.5 km (Figure 15a). Moreover, the layered model inversion also suggests that the top of unaltered mantle has a velocity around 7.9 km/s at a distance >280 km (Figure 2a). Another suspected weak reflector picked around 230 km distance also follows the C7.9 (white curve with a question mark in Figure 13b). Furthermore, the vertical gradient plot (Figure 10a) shows much lower gradients below the C7.9 than above at most model areas, consistent with the presence of low-gradient mantle layers below this contour. In conclusion, since 7.9 km/s indicates unaltered mantle rocks (e.g., Miller & Christensen, 1997) and the model C7.9 roughly coincides with weak sub-horizontal reflectors and/or changes in vertical gradient in the FWI model, we use the C7.9 as a proxy for the top of unaltered mantle (Figure 15a). However, we do not observe sharp reflections or strong vertical gradients between C7.2 and C7.9 that would suggest a prominent transition zone indicative of a typical Moho interface defined as rapid velocity increase from crustal-like (≤7.2 km/s) to mantle (≥7.9 km/s) velocities. Instead, the thickness between C7.2 and C7.9 is >2 km for most model areas (Figure 15b), and the synthetic test (Figure 12) suggests that our OBS FWI modeling would be able to recover a sharp MTZ if it were present.

5. Interpretation and Discussion

5.1. Rift to Drift Transition Zone

Following the morphological characteristics of the well-imaged top basement reflection and considering the bright reflection packages associated with the basement top at distances >236 km, we divide the basement into four domains that we interpret as representative of different stages of continental rifting/drifting (Figure 13b):

1. Domain I at model distance < 236 km, characterized by a single reflection from the top basement and smooth topography.
2. Domain II at 236–246 km model distance, representing a narrow area consisting of a small tilted block bounded by listric faults (Lister et al., 1991). Within the valleys on both sides of the block, there are packages of layered and bright continentward-dipping reflectors (CDR) (Gillard et al., 2017).
3. Domain III (246–262 km model distance) that has a shallower, relatively smooth basement topography cut by dense, small-throw faults. Immediately below the basement top, chaotic bright reflection packages are observed up to 2–3 km depth below basement.
4. Domain IV, located seaward of Domain III (>262 km model distance) and separated from it by two deep-cutting seaward-dipping normal faults and a 1 km-deep basement valley. In this domain, the basement has higher relief and locally thicker reflection packages below the basement top, and the weak reflection from the top of unaltered mantle is imaged.

5.1.1. Domain I

The Domain I basement has a 2.2–3.5 km-thick layer with velocities of 7.2–7.9 km/s (Figures 14a and 15b), which is consistent with a partially serpentinized mantle layer with serpentinization degree between 0% and 25% (Miller & Christensen, 1997). The upper basement layer (5.3–7.2 km/s) is thicker (2.8–5.5 km) and it may be composed of remanent continental crust, exhumed highly serpentinized mantle (ESM) or volcanic materials. An ESM upper basement layer is well documented at the Western Iberia margin, where the basement is revealed as an unreflective layer overlying a reflective layer, corresponding to highly and partially serpentinized mantle rocks, respectively (Pickup et al., 1996). However, we do not observe such an unreflective layer and the upper basement velocity seems too high in comparison to the ESM layer observed at the Iberia margin (Chian et al., 1999; Minshull et al., 2014). The presence of volcanic materials in the upper basement layer cannot be completely excluded by our results, but we suggest that the percentage must be low because the single reflection event of the top basement and the relatively transparent basement interior clearly differ from the thick reflection packages in more distal domains that are indicative of magmatic additions. Therefore, we suggest that the Domain I is mainly composed of remnant continental crust overlying or mixed with serpentinized mantle. The maximum velocity expected in continental crust does not exceed 7.2 km/s (Christensen & Mooney, 1995). If we assume all materials between C5.3 and C7.2 are remnant continental crust, it has a thickness ~5 km at 205 km distance, <4 km at 215 km distance, and <3 km at 240 km, indicating rapid seaward thinning. Considering that part of the materials with these velocities may be serpentinized mantle, the actual crustal thickness is likely even smaller, suggesting hyperextension of the continental crust whose pre-rift thickness is about 34 km (Barrett et al., 1964).

If our interpretation of the Domain I consisting of remanent continental crust is correct, the very limited extension that can be attributed to the imaged faults accounts for only a fraction of the inferred continental crustal thinning. This discrepancy can be explained by a polyphase extension mode (Lavier & Manatschal, 2006; Peron-Pinvidic et al., 2013; Reston, 2009), where early stage faulting is obscured by later-stage faults and invisible in the seismic image (McDermott & Reston, 2015). This may also explain why there are no angular blocks generated by listric faults that are typical for rifted continental crust, if different faulting phases have alternating polarities (Reston & McDermott, 2011). Depth-dependent extension, where the lower crust is transported away together with the mantle lithosphere before the upper continental crust breaks up (Brune et al., 2014; Huismans & Beaumont, 2014; Kusznir & Karner, 2007; Sutra & Manatschal, 2012), can also thin the crust significantly without leaving tell-tell signs that can be identified on reflection images. The transportation of lower crust and lithospheric mantle could be symmetric (e.g., Huismans & Beaumont) or asymmetric (e.g., Brune et al., 2014) on the conjugate margins, depending on the thermal and rheological status of the lithosphere during the rifting. A consequence of this model is the early asthenospheric upwelling, resulting in magmatism accompanying the upper continental breakup and the onset of seafloor spreading immediately after the breakup, without creating vast exhumation of mantle rocks.

5.1.2. Domain II

The tilted block in the Domain II is interpreted as a rider block of continental crust, because of its triangular shape and the transparent interior that are distinct from the characteristics of neighboring CDRs on both sides. The neighboring bright and layered CDRs have seismic velocities of 5–6.5 km/s (Figures 14b and 13), which are likely to be synrift extrusive magmatic layers rather than sediments, because they are localized features and the velocity is much higher than for any sediment units in our model. Both of these arguments also exclude the possibility that these CDRs represent metasediments. Similar reflectors are also observed at the Gulf of Guinea magma-poor rifted margin and interpreted as magmatic extrusive bodies emplaced in a transitional domain prior to lithospheric breakup (Gillard et al., 2017).

Throughout the Domain II, there is a bright subhorizontal reflector at 2–3 km below the top basement (H2 in Figure 13). It connects to another bright reflector, H1 in Domain I, with a weak subhorizontal reflector (dotted green curve in Figure 13). These reflectors are clearly observable in Figure S9b in Supporting Information S1, where no interpretation is carried out. No normal faults cut through these subhorizontal reflectors, suggesting that they may be the decollement level during the late stage of continental rifting. The vertical velocity gradient also shows systematic decreases below those reflectors (Figure 13b). Gillard et al. (2019) review similar subhorizontal reflectors below ESM sections at magma-poor rifted margins, and propose that the reflectors at about 3 km below the basement top may result from deformation localized in a decollement level due to the abrupt change in the mechanical behavior of peridotites when they are serpentinized to 10%–15% (Escartín et al., 2001). While the 10%–15% degree of serpentinization corresponds to velocities of 7.5–7.8 km/s, our results show that the H1-H2 reflector system corresponds to seismic velocities of 6.5–7.2 km/s (Figure 13a). This discrepancy may be related to the presence of remanent continental crust in our study area, in contrast to the ESM on the basement top in the study area of Gillard et al. (2019), and the H1-H2 reflection may correspond to weak crustal materials or the crust and serpentinized mantle boundary.

On the other hand, the H2 reflector may also correspond to a small amount of magmatic underplate that is responsible for the formation of the overlying extrusive CDRs. Immediately above the H2, there is a thin layer of very high vertical gradients (Figure 13b), where the velocity rapidly increase from 5 to 6.5 km/s in the extrusive CDR layers to a 2–3 km thick, low-gradient layer with velocities of 7–7.3 km/s (Figure 14b) that may be formed by gabbroic intrusions into the serpentinized mantle (e.g., Dunn et al., 2017). If this is correct, the lower continental crust in the Domain II could have ruptured or been squeezed out before the upper continental crust broke up, and the mantle underlying the Domain I and II was infiltrated with interstitial melt before the melt bodies accumulated and finally erupted in the Domain II. Thus, some isolated reflectors may be related to small intrusion bodies in the Domain I mantle.

5.1.3. Domain III

Seaward of the Domain II, the CDRs are truncated by the fault F23 (Figure 13b), across which the basement characteristics change abruptly from the layered CDRs to less bright, chaotic reflector packages in the Domain III. The basement is shallower and has a low relief. The upper basement velocity contours (C5.3–C6.5) are correlated to the basement topography whereas the lower basement contours (C7.0-C7.2) are anticorrelated (Figures 13a and 15a), creating a thicker layer between C6.5 and C7.2 with lower vertical velocity gradients (Figures 13b and 14c). These features are best interpreted by more intrusive bodies due to increased magmatism (e.g., Canales et al., 2000; Dunn et al., 2017; Jian et al., 2016). We suggest that the Domain III is more magmatically dominated, with the upper basement mainly consisting of volcanic materials. This is also consistent with a weak positive magnetic anomaly (Figures 15c and 1b). We propose that the Domain II corresponds to the final step in the continental breakup and the Domain III represents the first domain containing little or no continental crust material. This interpretation suggests that the fault F23 may represent the continent-ocean boundary (COB). The presence of volcanic materials on both sides of the COB suggests that a magmatic event may assist in both the continental breakup and the crustal accretion in the embryonic oceanic spreading.

An ~8-km-long horizontal reflector (H3 in Figure 13b) is imaged in the Domain III, corresponding to velocities of 6.8–7 km/s. It may represent intruded sills, or the base of the volcanic basement separating it from the underlain serpentinized mantle. If H3 is related to sills, its great length would suggest the presence of a steady-state magma chamber at about 3 km depth below the basement top, which is comparable to what is observed at magmatic segment centers of the slow and ultraslow spreading ridges (e.g., Jian et al., 2017; Seher et al., 2010; Singh

et al., 2006), and thus a thick (>4 km) oceanic layer 3 with low velocity gradients would be expected to accommodate the excess melt that crystallized in situ (Henstock et al., 1993; Morgan & Chen, 1993). We do not observe such a layer, so we prefer to interpret the reflector as a lithological transition between magmatic materials and partially serpentinized mantle. The melt may be transported from mantle reservoirs through rapid dyke injections without creating shallow magma chambers and a gabbroic lower crust (Cannat et al., 2019).

Domain III is terminated on the seaward side by a 5 km-wide basement valley hosting two deep-cutting normal faults. Beneath the valley, reflector sequences are observed at large depths, among which some isolated reflectors are extremely bright. Lau et al. (2019) analyzed a margin-parallel seismic profile that crosses our seismic profile at 267 km distance. Around the intersection point, the margin-parallel profile reveals a northeast-dipping reflector from the basement top down to 14 km depth. This reflector is interpreted by these authors as separating the oceanic crust to the northeast and the serpentinized mantle to the southwest. Thus, we speculate that the complex image beneath the basement valley arises from 3-D structures. Overall, the deep valley and large faults suggest subdued magmatism in comparison to the Domain III, indicating the termination of the magmatic event associated with the continental breakup.

5.1.4. Domain IV

In Domain IV, a weak subhorizontal reflector is imaged around the velocity contour of 7.9 km/s (dashed white line in Figure 13), which may correspond to the top of unaltered mantle. Within the basement, the seismic image reveals some volcanic layers near the top basement, normal faults, and a possible intruded sill (Figure 13b) that are comparable to what is observed in the crust formed at magma-poor slow/ultraslow spreading mid-ocean ridges. This domain and the area further seaward are interpreted to have been generated by seafloor spreading with varying magmatic and tectonic contributions.

5.2. Magma-Poor Seafloor Spreading

At model distance >270 km, the layered model of Lau et al. (2018) includes a typical oceanic crustal structure composed of layer 2 and 3 overlying unaltered mantle, with a Moho interface with sharp velocity jumps from about 7.2 km/s to 7.9–8 km/s (Figures 2a and 14e–14g). However, our FWI model clearly differs, showing a layer with velocities of 7.2–7.9 km that is >2 km thick at most places (Figure 15b). Unlike the layered model building that relies on the presumed interfaces, our inversion routine is more data-driven and only reconstructs interfaces when corresponding triplications coherently exist in the data. For example, the sharp transition across the top basement is well resolved along the full length of the model because the data contain coherent triplications from this interface (Figure 8 and Figures S1–S5 in Supporting Information S1). In contrast, we do not find any widely observed thin transition zones or high-gradient layers from 7.2 to 7.9 km/s that may indicate a sharp MTZ (Figure 10) because PmP triplications observed in OBS data in this part of the model are weak and intermittent. More importantly, the synthetic test (Figure 12) demonstrates that the FWI is capable of reconstructing sharp transition zones at the possible Moho depths. Thus, the >2 km-thick layer between C7.2 and C7.9 is a robust feature required by the data, not an artifact due to the smoothing regularization. We believe a sharp MTZ is systematically absent in our observed oceanic zone.

The spreading rates during the early stages of the central North Atlantic Ocean drifting fall within the ultraslow to slow spreading range (Schettino & Turco, 2009; Labails et al., 2010). With slower spreading rates, the oceanic crustal structures are more divergent (Chen, 1992; Li et al., 2015). At slow/ultraslow ridge segments, magmatic centers hosting a crustal magma chamber can have crustal thickness of up to 7–9.5 km composed of a 3-4 km-thick layer 2 and a thicker layer 3 (e.g., Canales et al., 2000; Dunn et al., 2005; Jian et al., 2016; Seher et al., 2010). However, at discontinuities or magma-starved segments, the oceanic crust is a thin layer consisting of mixed volcanic rocks and serpentinized mantle rocks (Cannat, 1993; Dunn et al., 2017) or it disappears altogether so that the mantle is exhumed on the seafloor (Corbalán et al., 2021; Sauter et al., 2013). In our study area, the layered model suggests a magmatic crustal thickness of 3.5–6 km (Lau et al., 2018), whereas our model suggests a magmatic crustal thickness of mostly 2–4 km if we assume all the velocities of 5.3–7.2 km/s are attributed to magmatic sources (Figure 15b). In both models, the crust is too thin to have been accreted from a steady crustal magma chamber under the slow/ultraslow spreading rate. Instead, the models suggest an oceanic crust formed under a magma-poor environment where the layer 3 is very thin or absent and a highly fractured volcanic layer

overlays serpentinized mantle (Canales et al., 2000). This would explain the nearly uniform velocity gradient from the top basement to the unaltered mantle (Figures 14e–14h) and the absence of a sharp MTZ.

Considering that the magmatic layer is very thin, serpentinization has likely been pervasive and responsible for the formation of the layer between C7.2 and C7.9. Based on the observations and models from magma-poor slow/ultraslow spreading ridge segments, we suggest that the melt feeding the volcanic layer may have migrated from neighboring magmatic centers through lateral dyke propagation (Buck et al., 2006). Such magmatic centers may be located at the center of neighboring positive magnetic anomaly centers that are 10–30 km away from the profile (Figure 1b). However, it is also possible that melt upwells directly to form the volcanic layer and intrudes into the serpentinized mantle, similar to what is proposed for non-transform discontinuities of the Mid-Atlantic Ridge (Canales et al., 2017).

The crustal accretion process under slow/ultraslow spreading is episodic, with variable melt supply. Despite the oceanic spreading that is generally magma-poor, we can still identify several areas with slightly greater magma supply where the basement top is elevated and the thickness between C5.3 and C7.2 is larger (Figure 15). The breakup magmatic event ends at 260 km. The following relatively magmatic episode restarts from 277 km distance and ends at 296 km, generating a thicker volcanic layer that corresponds to a wider magnetic anomaly. A smaller magmatic episode lies between 336 and 348 km with less pronounced signatures. The last one is at the seaward end of the profile and extends to a wider range beyond the profile, as suggested by the wide and strong magnetic anomaly M25 (Figure 1b). On the other hand, the tectonic effect is anticorrelated to the magmatism, due to the thermal and mechanical response of lithosphere to the magmatism. Figure 15b illustrates this relationship using the anticorrelation between the thickness of C5.3-C7.2 and C7.2-C7.9. In particular, there is an extremely tectonically dominated episode between 312 and 332 km, where the basement topography, the undulation of velocity contours for <6.5 km/s (Figure 15a) and the velocity gradients (Figure 10) suggest the presence of deep-cutting faults, and the sink of velocity contours for ≥7.5 km/s may suggest higher serpentinization degrees due to these large faults (Bayrakci et al., 2016; Prada et al., 2017).

5.3. Comparison to Other Magma-Poor Margins

Several recent studies focused on the distal parts of magma-poor margins demonstrate the importance of magmatism at the rift to drift transition, even at the magma-poor margins. For example, Gillard et al. (2017) discover the CDRs at the Gulf of Guinea margin, and suggest that the onset of oceanic spreading is associated with the formation of a hybrid crust where continental crust and/or serpentinized mantle is sandwiched between magmatic intrusive and extrusive bodies. Our interpretation in the Domain II shows great similarities to that interpretation, as we interpret both magmatic extrusions overlying the continental block and magmatic underplating below the block around the H2 reflector. Based on the seismic reflection images from the magma-poor Australia-Antarctica margins, Gillard et al. (2015) propose a gradual transition from tectonic-driven rifting to magmatic-driven process through a proto-oceanic spreading domain formed by complex interaction between polyphase faulting and magmatism. In our models, although we interpret a COB between the Domain II and Domain III, the Domain III and IV are still dominated by tectonic extension. We do not observe a magma-dominated spreading phase in our study area that is comparable to what observed at magmatic segment centers of slow/ultraslow spreading ridges. Therefore, we cannot determine whether the Domain IV is under a proto-oceanic spreading phase that is followed by a magmatic-driven phase further seaward, or it is located at a magma-poor portion due to the along-axis variation of melt supply. However, the second interpretation is favored, because the margin-parallel seismic velocity model crossing the landward end of Domain IV does show strong short-wavelength (50 km) variations in crustal structure, which is comparable to the observation at Mid-Atlantic Ridge (Lau et al., 2019).

In contrast to the gradual transition process, a set of studies at the South China Sea rifted margin discover COBs where decompression melting is triggered to form mid-ocean ridge type magmatism and emplace both deep intrusive and shallow extrusive magmatic rocks, resulting in rapid transition from continental breakup to magmatic-driven oceanic spreading (e.g., Ding et al., 2020; Larsen et al., 2018; Nirrengarten et al., 2020). The magmatism associated with the breakup and the initial oceanic spreading in our study area is much smaller than that at the South China Sea margin, which may be related to the slower spreading rate and/or a colder mantle. In conclusion, magmatism accompanying continental breakup at the magma-poor margins is not rare. While this magmatism is a short-period event (Ding et al., 2020), the initial oceanic spreading following the continental breakup is controlled by the interaction of faulting, magma supply, and spreading rates (Nirrengarten et al., 2020).

6. Conclusions

Sparse wide-angle seismic profiling (OBS spacing 10–40 km), with data analysis using layered modeling or traveltime tomography, has been instrumental for advancing our knowledge about the regional structure of the COT at rifted margins. Despite these achievements, features of critical importance for understanding rifting processes, like the role of magmatism in magma-poor rifting, remain poorly constrained. Here, we apply FWI to OETR-2009 high-density (OBS spacing between <3 km and >10 km) wide-angle seismic data, and PSDM to GXT 2000 MCS data to derive a coincident high-resolution crustal-scale seismic velocity model and reflection image of the COT offshore northeastern Nova Scotia, the first such result at the Eastern North America Margin. This allows us to carry out interpretation of the structures related to the final stages of continental breakup and incipient oceanic accretion in greater detail than previously possible.

The COT is divided into four domains. The Domain I (205–236 km model distance) is interpreted as seaward-thinning (>5 to <3 km) hyperextended continental crust overlying a ∼2–3.5 km-thick partially serpentinized mantle layer. The hyperextension is caused by polyphase rifting, depth-dependent extension, or both. The ∼10-km-wide Domain II (236–246 km) includes a rider block of continental crust and synrift CDR sequences that are indicative of magmatic extrusive layers. The decollement reflector beneath Domain II is very bright and may also correspond to magmatic underplating that fed the overlying extrusions and promoted the continental rupture. The CDRs are truncated seaward by a major listric fault F23, here interpreted to represent the continent-ocean boundary that leads to the 16-km-wide Domain III (246–262 km). The basement topography is uplifted and smoother in Domain III as it is cut by dense but small-throw faults, and the top basement reflectivity characteristics change abruptly from bright and layered to dimmer and chaotic. The higher velocities at the top basement and lower vertical velocity gradients in the upper 3–4 km of the basement suggest that Domain III represents the breakup magmatic event that created embryonic oceanic crust with thin volcanic layers overlying a partially serpentinized mantle layer. Further seaward, a 5-km-wide basement valley hosting two deep-cutting faults separates Domain III from Domain IV (>262 km). Domain IV has a crustal thickness of only 2–4 km resulting from slow/ultraslow magma-poor oceanic spreading with variable melt supply.

Data Availability Statement

OETR-2009 wide-angle data and FWI velocity model, as well as the GXT-2000 PSDM data and image used in this paper are available for download at the National Facility for Seismic Imaging website (www.nfsi.ca).

Acknowledgments
H. Jian was supported by the Ocean Frontier Institute International Postdoctoral Fellowship at Dalhousie University and NSF grant OCE-2001012. The computation was performed on the DIG cluster at Dalhousie University and the Poseidon cluster at Woods Hole Oceanographic Institution. We are grateful to ION for the use of their GXT-2000 (NovaSPAN) data and prestack depth-migrated section. We would like to thank an associate editor and two anonymous reviewers, whose comments greatly improved the manuscript. We used Paradigm Echo for seismic data processing, and MATLAB and GMT for data analysis and presentation.

References

Arnulf, A. F., Harding, A. J., Singh, S. C., Kent, G. M., & Crawford, W. C. (2014). Nature of upper crust beneath the Lucky Strike volcano using elastic full waveform inversion of streamer data. *Geophysical Journal International*, *196*(3), 1471–1491. https://doi.org/10.1093/gji/ggt461

Barnes, C., & Charara, M. (2009). The domain of applicability of acoustic full-waveform inversion for marine seismic data. *Geophysics*, *74*(6), WCC91–WCC103. https://doi.org/10.1190/1.3250269

Barr, S. M., & Raeside, R. P. (1989). Tectono-stratigraphic terranes in Cape Breton Island, Nova Scotia: Implications for the configuration of the northern Appalachian orogen. *Geology*, *17*(9), 822–825. https://doi.org/10.1130/0091-7613(1989)017<0822:TSTICB>2.3.CO;2

Barrett, D. L., Berry, M., Blanchard, J. E., Keen, M. J., & McAllister, R. E. (1964). Seismic studies on the eastern seaboard of Canada: The Atlantic Coast of Nova Scotia. *Canadian Journal of Earth Sciences*, *1*, 10–22. https://doi.org/10.1139/e64-002

Bayrakci, G., Minshull, T. A., Sawyer, D. S., Reston, T. J., Klaeschen, D., Papenberg, C., et al. (2016). Fault-controlled hydration of the upper mantle during continental rifting. *Nature Geoscience*, *9*(5), 384–388. https://doi.org/10.1038/ngeo2671

Brenders, A. J., & Pratt, R. G. (2007). Efficient waveform tomography for lithospheric imaging: Implications for realistic, two-dimensional acquisition geometries and low-frequency data. *Geophysical Journal International*, *168*(1), 152–170. https://doi.org/10.1111/j.1365-246X.2006.03096.x

Brocher, T. M. (2005). Empirical relations between elastic wavespeeds and density in the Earth's crust. *Bulletin of the Seismological Society of America*, *95*(6), 2081–2092. https://doi.org/10.1785/0120050077

Bronner, A., Sauter, D., Manatschal, G., Péron-Pinvidic, G., & Munschy, M. (2011). Magmatic breakup as an explanation for magnetic anomalies at magma-poor rifted margins. *Nature Geoscience*, *4*(8), 549–553. https://doi.org/10.1038/ngeo1201

Bronner, A., Sauter, D., Munschy, M., Carlut, J., Searle, R., Cannat, M., & Manatschal, G. (2014). Magnetic signature of large exhumed mantle domains of the Southwest Indian Ridge – Results from a deep-tow geophysical survey over 0 to 11 Ma old seafloor. *Solid Earth*, *5*(1), 339–354. https://doi.org/10.5194/se-5-339-2014

Brune, S., Heine, C., Pérez-Gussinyé, M., & Sobolev, S. V. (2014). Rift migration explains continental margin asymmetry and crustal hyper-extension. *Nature Communications*, *5*(1), 4014. https://doi.org/10.1038/ncomms5014

Buck, W. R., Einarsson, P., & Brandsdóttir, B. (2006). Tectonic stress and magma chamber size as controls on dike propagation: Constraints from the 1975–1984 Krafla rifting episode. *Journal of Geophysical Research*, *111*(B12), B12404. https://doi.org/10.1029/2005JB003879

Bunks, C., Saleck, F. M., Zaleski, S., & Chavent, G. (1995). Multiscale seismic waveform inversion. *Geophysics*, *60*(5), 1457–1473. https://doi.org/10.1190/1.1443880

Canales, J. P., Detrick, R. S., Lin, J., Collins, J. A., & Toomey, D. R. (2000). Crustal and upper mantle seismic structure beneath the rift mountains and across a nontransform offset at the Mid-Atlantic Ridge (35°N). *Journal of Geophysical Research*, *105*(B2), 2699–2719. https://doi.org/10.1029/1999jb900379

Canales, J. P., Dunn, R. A., Arai, R., & Sohn, R. A. (2017). Seismic imaging of magma sills beneath an ultramafic-hosted hydrothermal system. *Geology*, *45*(5), 451–454. https://doi.org/10.1130/G38795.1

Cannat, M. (1993). Emplacement of mantle rocks in the seafloor at mid-ocean ridges. *Journal of Geophysical Research*, *98*(B3), 4163–4172. https://doi.org/10.1029/92JB02221

Cannat, M., Sauter, D., Lavier, L., Bickert, M., Momoh, E., & Leroy, S. (2019). On spreading modes and magma supply at slow and ultraslow mid-ocean ridges. *Earth and Planetary Science Letters*, *519*, 223–233. https://doi.org/10.1016/j.epsl.2019.05.012

Chen, Y. J. (1992). Oceanic crustal thickness versus spreading rate. *Geophysical Research Letters*, *19*(8), 753–756. https://doi.org/10.1029/92GL00161

Chian, D., Louden, K. E., Minshull, T. A., & Whitmarsh, R. B. (1999). Deep structure of the ocean-continent transition in the southern Iberia Abyssal Plain from seismic refraction profiles: Ocean Drilling Program (Legs 149 and 173) transect. *Journal of Geophysical Research*, *104*(B4), 7443–7462. https://doi.org/10.1029/1999JB900004

Christensen, N. I., & Mooney, W. D. (1995). Seismic velocity structure and composition of the continental crust: A global view. *Journal of Geophysical Research*, *100*(B6), 9761–9788. https://doi.org/10.1029/95JB00259

Christeson, G. L., Goff, J. A., & Reece, R. S. (2019). Synthesis of oceanic crustal structure from two-dimensional seismic profiles. *Reviews of Geophysics*, *57*(2), 504–529. https://doi.org/10.1029/2019RG000641

Claerbout, J. F. (1985). *Imaging the Earth's interior* (Vol. 1). Blackwell Scientific Publications.

Corbalán, A., Nedimović, M. R., Louden, K. E., Cannat, M., Grevemeyer, I., Watremez, L., & Leroy, S. (2021). Seismic velocity structure along and across the ultraslow-spreading southwest Indian Ridge at 64°30′E showcases flipping detachment faults. *Journal of Geophysical Research: Solid Earth*, *126*(10), e2021JB022177. https://doi.org/10.1029/2021JB022177

Davy, R. G., Minshull, T. A., Bayrakci, G., Bull, J. M., Klaeschen, D., Papenberg, C., et al. (2016). Continental hyperextension, mantle exhumation, and thin oceanic crust at the continent-ocean transition, West Iberia: New insights from wide-angle seismic. *Journal of Geophysical Research: Solid Earth*, *121*(5), 3177–3199. https://doi.org/10.1002/2016JB012825

Davy, R. G., Morgan, J. V., Minshull, T. A., Bayrakci, G., Bull, J. M., Klaeschen, D., et al. (2018). Resolving the fine-scale velocity structure of continental hyperextension at the Deep Galicia Margin using full-waveform inversion. *Geophysical Journal International*, *212*(1), 244–263. https://doi.org/10.1093/gji/ggx415

Dehler, S. A. (2012). Initial rifting and breakup between Nova Scotia and Morocco: Insight from new magnetic models. *Canadian Journal of Earth Sciences*, *49*(12), 1385–1394. https://doi.org/10.1139/e2012-073

Dehler, S. A., & Welford, J. K. (2013). Variations in rifting style and structure of the Scotian margin, Atlantic Canada, from 3D gravity inversion. *Geological Society, London, Special Publications*, *369*(1), 289–300. https://doi.org/10.1144/SP369.11

Deptuck, M. E., & Kendell, K. L. (2017). Chapter 13-A review of Mesozoic-Cenozoic salt tectonics along the Scotian margin, Eastern Canada. In J. I. Soto, J. F. Flinch, & G. Tari (Eds.), *Permo-Triassic salt provinces of Europe, North Africa and the Atlantic margins* (pp. 287–312). Elsevier. https://doi.org/10.1016/B978-0-12-809417-4.00014-8

Ding, W., Sun, Z., Mohn, G., Nirrengarten, M., Tugend, J., Manatschal, G., & Li, J. (2020). Lateral evolution of the rift-to-drift transition in the South China Sea: Evidence from multi-channel seismic data and IODP Expeditions 367&368 drilling results. *Earth and Planetary Science Letters*, *531*, 115932. https://doi.org/10.1016/j.epsl.2019.115932

Dunn, R. A., Arai, R., Eason, D. E., Canales, J. P., & Sohn, R. A. (2017). Three-dimensional seismic structure of the Mid-Atlantic Ridge: An investigation of tectonic, magmatic, and hydrothermal processes in the rainbow area. *Journal of Geophysical Research: Solid Earth*, *122*(12), 9580–9602. https://doi.org/10.1002/2017JB015051

Dunn, R. A., Lekić, V., Detrick, R. S., & Toomey, D. R. (2005). Three-dimensional seismic structure of the Mid-Atlantic Ridge (35°N): Evidence for focused melt supply and lower crustal dike injection. *Journal of Geophysical Research*, *110*(B9), B09101. https://doi.org/10.1029/2004JB003473

Escartín, J., Hirth, G., & Evans, B. (2001). Strength of slightly serpentinized peridotites: Implications for the tectonics of oceanic lithosphere. *Geology*, *29*(11), 1023–1026. https://doi.org/10.1130/0091-7613(2001)029<1023:SOSSPI>2.0.CO;2

Fletcher, R., & Reeves, C. M. (1964). Function minimization by conjugate gradients. *The Computer Journal*, *7*(2), 149–154. https://doi.org/10.1093/comjnl/7.2.149

Funck, T., Jackson, H. R., Louden, K. E., Dehler, S. A., & Wu, Y. (2004). Crustal structure of the northern Nova Scotia rifted continental margin (eastern Canada). *Journal of Geophysical Research*, *109*(B9), B09102. https://doi.org/10.1029/2004JB003008

Gerlings, J., Louden, K. E., Minshull, T. A., & Nedimović, M. R. (2012). Flemish Cap–Goban Spur conjugate margins: New evidence of asymmetry. *Geology*, *40*(12), 1107–1110. https://doi.org/10.1130/G33263.1

Gillard, M., Autin, J., Manatschal, G., Sauter, D., Munschy, M., & Schaming, M. (2015). Tectonomagmatic evolution of the final stages of rifting along the deep conjugate Australian-Antarctic magma-poor rifted margins: Constraints from seismic observations. *Tectonics*, *34*(4), 753–783. https://doi.org/10.1002/2015TC003850

Gillard, M., Sauter, D., Tugend, J., Tomasi, S., Epin, M.-E., & Manatschal, G. (2017). Birth of an oceanic spreading center at a magma-poor rift system. *Scientific Reports*, *7*(1), 15072. https://doi.org/10.1038/s41598-017-15522-2

Gillard, M., Tugend, J., Müntener, O., Manatschal, G., Karner, G. D., Autin, J., et al. (2019). The role of serpentinization and magmatism in the formation of decoupling interfaces at magma-poor rifted margins. *Earth-Science Reviews*, *196*, 102882. https://doi.org/10.1016/j.earscirev.2019.102882

Guan, H., Geoffroy, L., & Xu, M. (2021). Magma-assisted fragmentation of Pangea: Continental breakup initiation and propagation. *Gondwana Research*, *96*, 56–75. https://doi.org/10.1016/j.gr.2021.04.003

Henstock, T. J., Woods, A. W., & White, R. S. (1993). The accretion of oceanic crust by episodic sill intrusion. *Journal of Geophysical Research*, *98*(B3), 4143–4161. https://doi.org/10.1029/92JB02661

Hicks, G J. (2002). Arbitrary source and receiver positioning in finite-difference schemes using Kaiser windowed sinc functions. *Geophysics*, *67*(1), 156–165. https://doi.org/10.1190/1.1451454

Hinz, K., Mutter, J. C., & Zehnder, C. M. (1987). Symmetric conjugation of continent-ocean boundary structures along the Norwegian and East Greenland Margins. *Marine and Petroleum Geology*, *4*(3), 166–187. https://doi.org/10.1016/0264-8172(87)90043-2

Holbrook, W. S., & Kelemen, P. B. (1993). Large igneous province on the US Atlantic margin and implications for magmatism during continental breakup. *Nature*, *364*(6436), 433–436. https://doi.org/10.1038/364433a0

Huismans, R. S., & Beaumont, C. (2014). Rifted continental margins: The case for depth-dependent extension. *Earth and Planetary Science Letters*, *407*, 148–162. https://doi.org/10.1016/j.epsl.2014.09.032

Jian, H., Chen, Y. J., Singh, S. C., Li, J., Zhao, M., Ruan, A., & Qiu, X. (2016). Seismic structure and magmatic construction of crust at the ultraslow-spreading Southwest Indian Ridge at 50°28'E. *Journal of Geophysical Research: Solid Earth*, *122*(1), 18–42. https://doi.org/10.1002/2016JB013377

Jian, H., Singh, S. C., Chen, Y. J., & Li, J. (2017). Evidence of an axial magma chamber beneath the ultraslow-spreading Southwest Indian Ridge. *Geology*, *45*(2), 143–146. https://doi.org/10.1130/G38356.1

Kamei, R., Miyoshi, T., Pratt, R. G., Takanashi, M., & Masaya, S. (2015). Application of waveform tomography to a crooked-line 2D land seismic data set. *Geophysics*, *80*(5), B115–B129. https://doi.org/10.1190/geo2014-0537.1

Keen, C. E., & Potter, D. P. (1995). The transition from a volcanic to a nonvolcanic rifted margin off eastern Canada. *Tectonics*, *14*(2), 359–371. https://doi.org/10.1029/94TC03090

Klitgord, K. D., & Schouten, H. (1986). Plate kinematics of the central Atlantic. In P. R. Vogt, & B. E. Tucholke (Eds.), *The western north Atlantic region*. Geological Society of America.

Kusznir, N. J., & Karner, G. D. (2007). Continental lithospheric thinning and breakup in response to upwelling divergent mantle flow: Application to the Woodlark, Newfoundland and Iberia margins. *Geological Society, London, Special Publications*, *282*(1), 389–419. https://doi.org/10.1144/SP282.16

Labails, C., Olivet, J.-L., Aslanian, D., & Roest, W. R. (2010). An alternative early opening scenario for the Central Atlantic Ocean. *Earth and Planetary Science Letters*, *297*(3), 355–368. https://doi.org/10.1016/j.epsl.2010.06.024

Lailly, P. (1983). The seismic inverse problem as a sequence of before stack migrations. In *Conference on inverse scattering, theory and application, society for industrial and applied mathematics, expanded abstracts* (pp. 206–220).

Larsen, H. C., Mohn, G., Nirrengarten, M., Sun, Z., Stock, J., Jian, Z., et al. (2018). Rapid transition from continental breakup to igneous oceanic crust in the South China Sea. *Nature Geoscience*, *11*(10), 782–789. https://doi.org/10.1038/s41561-018-0198-1

Lau, K. W. H., Nedimović, M. R., & Louden, K. E. (2018). Continent-Ocean transition across the northeastern Nova Scotian margin from a dense wide-angle seismic profile. *Journal of Geophysical Research: Solid Earth*, *123*(5), 4331–4359. https://doi.org/10.1029/2017JB015282

Lau, K. W. H., Nedimović, M. R., & Louden, K. E. (2019). Along-strike variations in structure of the continent-ocean transition at the northeastern Nova Scotia margin from wide-angle seismic observations. *Journal of Geophysical Research: Solid Earth*, *124*(3), 3172–3196. https://doi.org/10.1029/2018JB016894

Lavier, L. L., & Manatschal, G. (2006). A mechanism to thin the continental lithosphere at magma-poor margins. *Nature*, *440*(7082), 324–328. https://doi.org/10.1038/nature04608

Levander, A. R. (1988). Fourth-order finite-difference P-SV seismograms. *Geophysics*, *53*(11), 1425–1436. https://doi.org/10.1190/1.1442422

Li, J., Jian, H., Chen, Y. J., Singh, S. C., Ruan, A., Qiu, X., et al. (2015). Seismic observation of an extremely magmatic accretion at the ultraslow spreading Southwest Indian Ridge. *Geophysical Research Letters*, *42*(8), 2656–2663. https://doi.org/10.1002/2014GL062521

Lin, J., Purdy, G. M., Schouten, H., Sempere, J.-C., & Zervas, C. (1990). Evidence from gravity data for focused magmatic accretion along the Mid-Atlantic Ridge. *Nature*, *344*(6267), 627–632. https://doi.org/10.1038/344627a0

Lister, G. S., Etheridge, M. A., & Symonds, P. A. (1991). Detachment models for the formation of passive continental margins. *Tectonics*, *10*(5), 1038–1064. https://doi.org/10.1029/90TC01007

Louden, K., Wu, Y., & Tari, G. (2013). Systematic variations in basement morphology and rifting geometry along the Nova Scotia and Morocco conjugate margins. *Geological Society, London, Special Publications*, *369*(1), 267–287. https://doi.org/10.1144/SP369.9

McDermott, K., & Reston, T. (2015). To see, or not to see? Rifted margin extension. *Geology*, *43*(11), 967–970. https://doi.org/10.1130/G36982.1

Miller, D. J., & Christensen, N. I. (1997). Seismic velocities of lower crustal and upper mantle rocks from the slow-spreading Mid-Atlantic Ridge, south of the Kane Transform Zone (MARK). In *Proceedings-ocean drilling program scientific results* (pp. 437–456). https://doi.org/10.2973/odp.proc.sr.153.043.1997

Minshull, T. A., Dean, S. M., & Whitmarsh, R. B. (2014). The peridotite ridge province in the southern Iberia Abyssal Plain: Seismic constraints revisited. *Journal of Geophysical Research: Solid Earth*, *119*(3), 1580–1598. https://doi.org/10.1002/2014JB011011

Mora, P. (1987). Nonlinear two-dimensional elastic inversion of multioffset seismic data. *Geophysics*, *52*(9), 1211–1228. https://doi.org/10.1190/1.1442384

Mora, P. (1989). Inversion = migration + tomography. *Geophysics*, *54*(12), 1575–1586. https://doi.org/10.1190/1.1442625

Morgan, J. P., & Chen, Y. J. (1993). Dependence of ridge-axis morphology on magma supply and spreading rate. *Nature*, *364*(6439), 706–708. https://doi.org/10.1038/364706a0

Moser, T. J. (1991). Shortest path calculation of seismic rays. *Geophysics*, *56*(1), 59–67. https://doi.org/10.1190/1.1442958

Nirrengarten, M., Mohn, G., Kusznir, N. J., Sapin, F., Despinois, F., Pubellier, M., et al. (2020). Extension modes and breakup processes of the southeast China-Northwest Palawan conjugate rifted margins. *Marine and Petroleum Geology*, *113*, 104123. https://doi.org/10.1016/j.marpetgeo.2019.104123

Oakey, G., & Dehler, S. (2004). *Atlantic Canada magnetic map series: Scotian Shelf and surrounds* (No. Open File Rep. 1814). Geological Survey of Canada

Ogg, J. G., Ogg, G., & Gradstein, F. M. (2016). *A concise geologic time scale: 2016*. Elsevier.

Peron-Pinvidic, G., Manatschal, G., & Osmundsen, P. T. (2013). Structural comparison of archetypal Atlantic rifted margins: A review of observations and concepts. *Marine and Petroleum Geology*, *43*, 21–47. https://doi.org/10.1016/j.marpetgeo.2013.02.002

Pica, A., Diet, J. P., & Tarantola, A. (1990). Nonlinear inversion of seismic reflection data in a laterally invariant medium. *Geophysics*, *55*(3), 284–292. https://doi.org/10.1190/1.1442836

Pickup, S. L. B., Whitmarsh, R. B., Fowler, C. M. R., & Reston, T. J. (1996). Insight into the nature of the ocean-continent transition off West Iberia from a deep multichannel seismic reflection profile. *Geology*, *24*(12), 1079–1082. https://doi.org/10.1130/0091-7613(1996)024<1079:IITNOT>2.3.CO;2

Prada, M., Watremez, L., Chen, C., O'Reilly, B. M., Minshull, T. A., Reston, T. J., et al. (2017). Crustal strain-dependent serpentinisation in the Porcupine Basin, offshore Ireland. *Earth and Planetary Science Letters*, *474*, 148–159. https://doi.org/10.1016/j.epsl.2017.06.040

Quirk, D. G., Shakerley, A., & Howe, M. J. (2014). A mechanism for construction of volcanic rifted margins during continental breakup. *Geology*, *42*(12), 1079–1082. https://doi.org/10.1130/G35974.1

Reston, T. J. (2009). The extension discrepancy and syn-rift subsidence deficit at rifted margins. *Petroleum Geoscience*, *15*(3), 217–237. https://doi.org/10.1144/1354-079309-845

Reston, T. J., & McDermott, K. G. (2011). Successive detachment faults and mantle unroofing at magma-poor rifted margins. *Geology*, *39*(11), 1071–1074. https://doi.org/10.1130/G32428.1

Sauter, D., Cannat, M., & Mendel, V. (2008). Magnetization of 0–26.5 Ma seafloor at the ultraslow spreading Southwest Indian Ridge, 61°–67°E. *Geochemistry, Geophysics, Geosystems*, *9*(4), Q04023. https://doi.org/10.1029/2007GC001764

Sauter, D., Cannat, M., Rouméjon, S., Andreani, M., Birot, D., Bronner, A., et al. (2013). Continuous exhumation of mantle-derived rocks at the Southwest Indian Ridge for 11 million years. *Nature Geoscience*, *6*(4), 314–320. https://doi.org/10.1038/ngeo1771

Schettino, A., & Turco, E. (2009). Breakup of Pangaea and plate kinematics of the central Atlantic and Atlas regions. *Geophysical Journal International*, *178*(2), 1078–1097. https://doi.org/10.1111/j.1365-246X.2009.04186.x

Seher, T., Crawford, W. C., Singh, S. C., Cannat, M., Combier, V., & Dusunur, D. (2010). Crustal velocity structure of the Lucky Strike segment of the Mid-Atlantic Ridge at 37°N from seismic refraction measurements. *Journal of Geophysical Research*, *115*(B3), B03103. https://doi.org/10.1029/2009JB006650

Seton, M., Müller, R. D., Zahirovic, S., Williams, S., Wright, N. M., Cannon, J., et al. (2020). A global data set of present-day oceanic crustal age and seafloor spreading parameters. *Geochemistry, Geophysics, Geosystems*, *21*(10), e2020GC009214. https://doi.org/10.1029/2020GC009214

Shimeld, J. (2004). A comparison of salt tectonic subprovinces beneath the Scotian Slope and Laurentian Fan. In *24th annual GCS-SEPM foundation bob f. Perkins research conference, Houston* (pp. 291–306). https://doi.org/10.5724/gcs.04.24.0502

Shipp, R. M., & Singh, S. C. (2002). Two-dimensional full wavefield inversion of wide-aperture marine seismic streamer data. *Geophysical Journal International*, *151*(2), 325–344. https://doi.org/10.1046/j.1365-246X.2002.01645.x

Sibuet, J.-C., Rouzo, S., & Srivastava, S. (2012). Plate tectonic reconstructions and paleogeographic maps of the central and North Atlantic oceans. *Canadian Journal of Earth Sciences*, *49*(12), 1395–1415. https://doi.org/10.1139/e2012-071

Sibuet, J.-C., Srivastava, S., & Manatschal, G. (2007). Exhumed mantle-forming transitional crust in the Newfoundland-Iberia rift and associated magnetic anomalies. *Journal of Geophysical Research*, *112*(B6), B06105. https://doi.org/10.1029/2005JB003856

Singh, S. C., Crawford, W. C., Carton, H., Seher, T., Combier, V., Cannat, M., et al. (2006). Discovery of a magma chamber and faults beneath a Mid-Atlantic Ridge hydrothermal field. *Nature*, *442*(7106), 1029–1032. https://doi.org/10.1038/nature05105

Sirgue, L., & Pratt, R. G. (2004). Efficient waveform inversion and imaging: A strategy for selecting temporal frequencies. *Geophysics*, *69*(1), 231–248. https://doi.org/10.1190/1.1649391

Sutra, E., & Manatschal, G. (2012). How does the continental crust thin in a hyperextended rifted margin? Insights from the Iberia margin. *Geology*, *40*(2), 139–142. https://doi.org/10.1130/G32786.1

Tarantola, A. (1984). Inversion of seismic reflection data in the acoustic approximation. *Geophysics*, *49*(8), 1259–1266. https://doi.org/10.1190/1.1441754

Tarantola, A. (1988). Theoretical background for the inversion of seismic waveforms including elasticity and attenuation. *Pure and Applied Geophysics*, *128*(1), 365–399. https://doi.org/10.1007/BF01772605

Tucholke, B. E., Sawyer, D. S., & Sibuet, J.-C. (2007). Breakup of the Newfoundland–Iberia rift. *Geological Society, London, Special Publications*, *282*(1), 9–46. https://doi.org/10.1144/SP282.2

Tugend, J., Gillard, M., Manatschal, G., Nirrengarten, M., Harkin, C., Epin, M.-E., et al. (2020). Reappraisal of the magma-rich versus magma-poor rifted margin archetypes. *Geological Society, London, Special Publications*, *476*(1), 23–47. https://doi.org/10.1144/SP476.9

Van Avendonk, H. J. A., Holbrook, W. S., Nunes, G. T., Shillington, D. J., Tucholke, B. E., Louden, K. E., et al. (2006). Seismic velocity structure of the rifted margin of the eastern Grand Banks of Newfoundland, Canada. *Journal of Geophysical Research*, *111*(B11), B11404. https://doi.org/10.1029/2005JB004156

Van Avendonk, H. J. A., Shillington, D. J., Holbrook, W. S., & Hornbach, M. J. (2004). Inferring crustal structure in the Aleutian island arc from a sparse wide-angle seismic data set. *Geochemistry, Geophysics, Geosystems*, *5*(8), Q08008. https://doi.org/10.1029/2003GC000664

Voss, M., Schmidt-Aursch, M. C., & Jokat, W. (2009). Variations in magmatic processes along the East Greenland volcanic margin. *Geophysical Journal International*, *177*(2), 755–782. https://doi.org/10.1111/j.1365-246X.2009.04077.x

Welford, J. K., Hall, J., Sibuet, J.-C., & Srivastava, S. P. (2010). Structure across the northeastern margin of Flemish Cap, offshore Newfoundland from Erable multichannel seismic reflection profiles: Evidence for a transtensional rifting environment. *Geophysical Journal International*, *183*(2), 572–586. https://doi.org/10.1111/j.1365-246X.2010.04779.x

Whitmarsh, R. B., Minshull, T. A., Russell, S. M., Dean, S. M., Louden, K. E., & Chian, D. (2001). The role of syn-rift magmatism in the rift-to-drift evolution of the West Iberia continental margin: Geophysical observations. *Geological Society, London, Special Publications*, *187*(1), 107–124. https://doi.org/10.1144/GSL.SP.2001.187.01.06

Williams, H. (1995). Temporal and spatial divisions. In *Geology of the Appalachian-Caledonian orogen in Canada and Greenland*. Geological Survey of Canada, Geology of Canada, 6, 23–44.

Wood, L. C., Heiser, R. C., Treitel, S., & Riley, P. L. (1978). The debubbling of marine source signatures. *Geophysics*, *43*(4), 715–729. https://doi.org/10.1190/1.1440848

Wu, R.-S., & Toksöz, M. N. (1987). Diffraction tomography and multisource holography applied to seismic imaging. *Geophysics*, *52*(1), 11–25. https://doi.org/10.1190/1.1442237

Wu, Y., Louden, K. E., Funck, T., Jackson, H. R., & Dehler, S. A. (2006). Crustal structure of the central Nova Scotia margin off Eastern Canada. *Geophysical Journal International*, *166*(2), 878–906. https://doi.org/10.1111/j.1365-246X.2006.02991.x

Xu, S., Wang, D., Chen, F., Zhang, Y., & Lambare, G. (2012). Full waveform inversion for reflected seismic data (p. cp). Presented at the 74th EAGE Conference and Exhibition incorporating EUROPEC 2012, European Association of Geoscientists & Engineers. https://doi.org/10.3997/2214-4609.20148725

Yang, P., Brossier, R., & Virieux, J. (2016). Wavefield reconstruction by interpolating significantly decimated boundaries. *Geophysics*, *81*(5), T197–T209. https://doi.org/10.1190/geo2015-0711.1

Zelt, C. A., Sain, K., Naumenko, J. V., & Sawyer, D. S. (2003). Assessment of crustal velocity models using seismic refraction and reflection tomography. *Geophysical Journal International*, *153*(3), 609–626. https://doi.org/10.1046/j.1365-246X.2003.01919.x

Zelt, C. A., & Smith, R. B. (1992). Seismic traveltime inversion for 2-D crustal velocity structure. *Geophysical Journal International*, *108*(1), 16–34. https://doi.org/10.1111/j.1365-246X.1992.tb00836.x